nature plants

Article

https://doi.org/10.1038/s41477-023-01500-2

Cryo-EM structures of LHCII in photo-active and photo-protecting states reveal allosteric regulation of light harvesting and excess energy dissipation

Received: 14 March 2023

Accepted: 26 July 2023

Check for updates

Meixia Ruan[1,2,7], Hao Li[3,4,7], Ying Zhang[1,2], Ruoqi Zhao[4], Jun Zhang[4], Yingjie Wang[4], Jiali Gao[3,4,5] ✉, Zhuan Wang[1], Yumei Wang[1], Dapeng Sun[1], Wei Ding[1,2] ✉ & Yuxiang Weng[1,2,6] ✉

The major light-harvesting complex of photosystem II (LHCII) has a dual regulatory function in a process called non-photochemical quenching to avoid the formation of reactive oxygen. LHCII undergoes reversible conformation transitions to switch between a light-harvesting state for excited-state energy transfer and an energy-quenching state for dissipating excess energy under full sunshine. Here we report cryo-electron microscopy structures of LHCII in membrane nanodiscs, which mimic in vivo LHCII, and in detergent solution at pH 7.8 and 5.4, respectively. We found that, under low pH conditions, the salt bridges at the lumenal side of LHCII are broken, accompanied by the formation of two local α-helices on the lumen side. The formation of α-helices in turn triggers allosterically global protein conformational change, resulting in a smaller crossing angle between transmembrane helices. The fluorescence decay rates corresponding to different conformational states follow the Dexter energy transfer mechanism with a characteristic transition distance of 5.6 Å between Lut1 and Chl612. The experimental observations are consistent with the computed electronic coupling strengths using multistate density function theory.

In green plants, the antenna light-harvesting complex of photosystem II (LHCII) not only absorbs and transports excitation energy towards the photosynthetic reaction centre but also serves as a site for energy dissipation[1–3]. The latter self-regulatory process is known as non-photochemical quenching (NPQ)[3–7] and is responsible for the conversion of excess photo-excitation energy under intense sunlight radiation into thermal energy to prevent photo-damage to the plant cells[8]. Although the phenomenological process is fully characterized, its molecular mechanism remains unknown. An understanding of the molecular mechanism regulating energy dissipation can provide the much-needed guidance in designing transgenic plants that regulate the NPQ process. For example, an acceleration of NPQ relaxation by genetic

[1]Laboratory of Soft Matter Physics, Institute of Physics, Chinese Academy of Sciences, Beijing, China. [2]University of Chinese Academy of Sciences, Beijing, China. [3]School of Chemical Biology and Biotechnology, Peking University Shenzhen Graduate School, Shenzhen, China. [4]Institute of Systems and Physical Biology, Shenzhen Bay Laboratory, Shenzhen, China. [5]Department of Chemistry and Supercomputing Institute, University of Minnesota, Minneapolis, MN, USA. [6]Songshan Lake Materials Laboratory, Dongguan, China. [7]These authors contributed equally: Meixia Ruan, Hao Li. ✉e-mail: gao@jialigao.org; dingwei@iphy.ac.cn; yxweng@iphy.ac.cn

https://doi.org/10.1038/s41477-023-01500-2

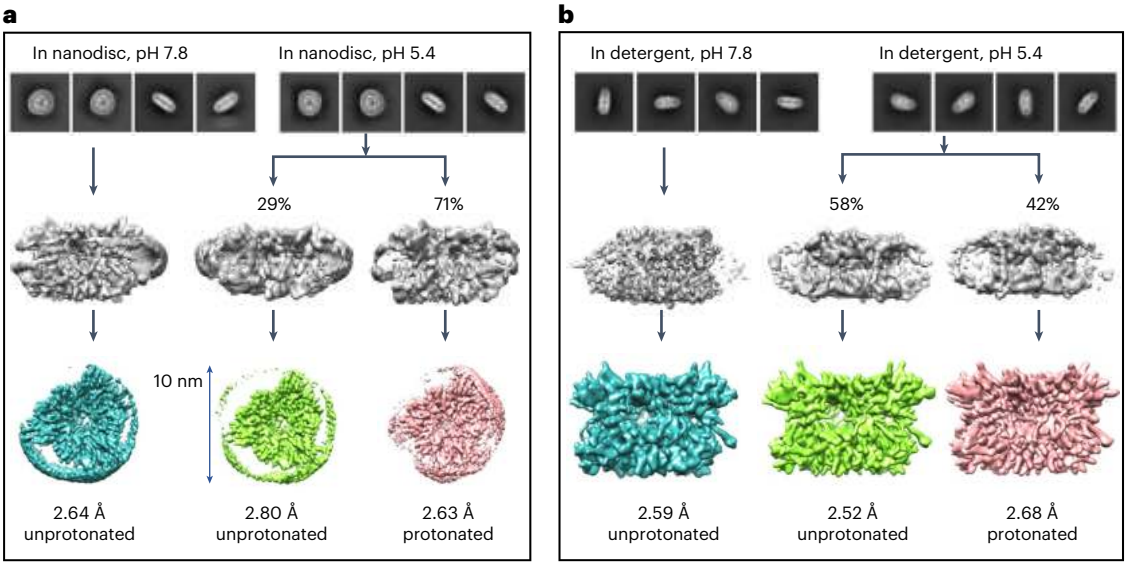

Fig. 1 | Cryo-EM structures of LHCII in nanodisc and in detergent solution. **a**, Two-dimensional and 3D images of LHCII embedded in 10 nm nanodisc. At high pH (7.8), a single 3D reconstruction density map for an unprotonated structure at a resolution of 2.64 Å is obtained. At low pH (5.4), two distinctive 3D structures can be identified: one unprotonated structure at a resolution of 2.80 Å, and the other protonated structure at a resolution of 2.63 Å. **b**, Two-dimensional and 3D images of LHCII in detergent solution. At high pH (7.8), a single 3D reconstruction density map for an unprotonated structure at a resolution of 2.59 Å is obtained. At low pH (5.4), there is one unprotonated structure at a resolution of 2.52 Å, and another protonated structure at a resolution of 2.68 Å. The top-view images with membrane scaffold protein are shown in **a**, whereas the side view is shown in **b**.

engineering can substantially increase biomass production by 33% in soybean[9] and 15% in tobacco[10]. The overall NPQ involves a multitude of interdependent processes across spatial and temporal scales, initiated by an increase in acidity in the lumen, leading to accumulation of the zeaxanthin (Zea) via the light-intensity-dependent xanthophyll cycle and PsbS-dependent aggregation of LHCII in the membrane. Here we report the cryo-electron microscopy (cryo-EM) structures of LHCII in its photo-active and photo-protecting states obtained under high (7.8) and low (5.4) pH conditions (Fig. 1). Analyses of these structures reveal an allosteric regulation mechanism for the interconversion between light-harvesting and energy-dissipating processes.

The crystal structures of the trimeric LHCII[11] show that each monomer consists of three transmembrane (TM) helices (helices A, B and C) and one amphiphilic helix (helix D), along with an amphoteric short 3_{10}-helix (helix E) at the lumenal side of the membrane (Fig. 2a). The crystal structures correspond to a photo-protecting state, reflected by a substantial reduction in the fluorescence lifetime of LHCII. In particular, the fluorescence decay of the non-aggregated LHCII trimer has an average lifetime of around 4 ns[12–14], which is decreased to a fast rate of energy quenching of 0.1–0.6 ns[15,16]. LHCII crystals show characteristic fluorescence lifetime signatures around 1 ns[11,17–19], partly due to crystal packing. The presence of an equilibrium between the photo-active and photo-protecting states was postulated on the basis of fluorescence decay kinetics[20] and single molecular spectroscopy[21,22]. In this work, we show an ensemble of six cryo-EM structures of LHCII trimer in detergent solution and confined in membrane nanodisc at different pH values, where the membrane confinement and pH values regulate the conformational transition between the light-harvesting and energy-quenching states, and we observed that LHCII confined in membrane nanodisc has different fluorescence lifetime signatures at different pH values. Together with the known crystal structures[11,23–26] of aggregated LHCII in a fluorescence-quenching state, the cryo-EM structures show the protein conformations responsible for light harvesting and energy quenching. These cryo-EM structures help identify LHCII allosteric conformational changes in response to the change in pH conditions and the effect of membrane confinement.

LHCII from spinach was purified at pH 6.5 and then solubilized in 0.03% (w/v) *n*-dodecyl β-D-maltoside (β-DDM) solution at a final pH adjusted to 7.8 and 5.4, respectively (Extended Data Fig. 1). LHCII nanodiscs were prepared by embedding a single LHCII trimer into a soybean lipid nanodisc, confined by membrane scaffold protein (MSP1E3D1), with a diameter of 10 nm as measured by cryo-EM single-particle imaging (Fig. 1a and Extended Data Fig. 1) at the same pH conditions. The corresponding fluorescence decay kinetics were determined using the time correlated single-photon counting method, and the fitted lifetimes under different conditions are listed in Extended Data Fig. 2.

We performed cryo-EM single-particle analysis of the LHCII in detergent solution and in nanodiscs at pH 7.8 and 5.4, resulting in a total of six structures. We differentiate these as unprotonated and protonated structures based on the protonation states of D54 and E207 at different acidic conditions (Fig. 2b,c), resulting in four unprotonated structures at pH 7.8 and 5.4, and two protonated structures at pH 5.4 (Fig. 1). After two-dimensional (2D) and three-dimensional (3D) classification of the cryo-EM images, the final 3D reconstruction maps for these six LHCII structures were refined to resolutions between 2.52 Å and 2.80 Å (Fig. 1 and Extended Data Figs. 3 and 4 and Extended Data Table 1). The density maps allowed us to build reliable models for the protein and all associated pigments.

Unprotonated and protonated conformations

Figure 2b,c and Extended Data Fig. 5a,b show the formation and disruption of the K203-E207 salt bridge at the lumenal side, and the hydrogen bond network of D54 at the stromal side of LHCII in nanodiscs and in detergent solution at pH 7.8 and pH 5.4; these results suggest the protonation of D54 and E207 after acidification. Figure 2b and Extended Data Fig. 5a only show the K203-E207 salt bridge in one monomer but the conformation of the salt bridge is identical in the other two subunits of the different structures (Extended Data Fig. 5c). The corresponding residue-density maps are shown in Extended Data Fig. 6. Hence, we classify these two different structures as unprotonated at pH 7.8 and protonated at pH 5.4 (Fig. 1). We then compared the protonated and unprotonated conformations of the LHCII nanodisc. Interestingly,

https://doi.org/10.1038/s41477-023-01500-2

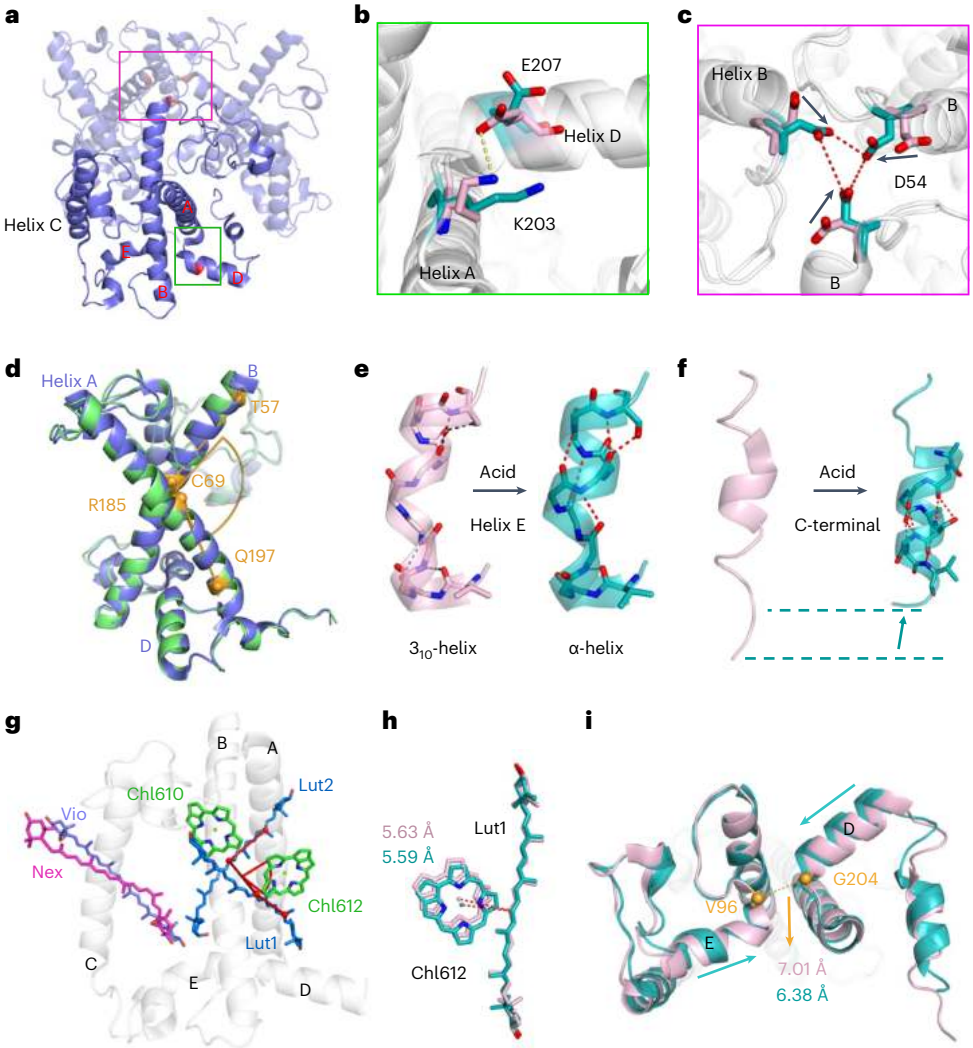

Fig. 2 | Protein secondary structures and pigments in different conformations. a, Structure of LHCII trimer (PDB: 1RWT) showing the locations of K203–K207 in a monomer at the lumenal side and D54 in three monomers in the stromal side, highlighted in green and pink boxes, respectively. **b**, Formation (dotted line) and disruption of the salt bridge between K203 and E207 in the unprotonated (pink) and protonated (teal) conformations of LHCII nanodisc. **c**, Formation and disruption of the hydrogen bond network among D54 of each monomer in the protonated and unprotonated conformations of LHCII nanodisc. The arrows indicate the inward motion of each D54 at the stromal side after protonation. **d**, Alignment of the crystal structure (blue; PDB: 1RWT) and cryo-EM structure of LHCII in detergent solution at pH 7.8 (green); the yellow spheres represent Cα of T57-C69-R185-Q197, which define the crossing angle of TM helices A and B. **e**, Structural comparison of helix E in LHCII nanodisc without and with acidification (pH 7.8, left; pH 5.4, right): a change from a 3_{10}-helix to an α-helix occurs. **f**, Structural comparison of the C-terminal in LHCII nanodisc without and with acidification (pH 7.8, left; pH 5.4, right): a change from C-terminal random coil into an α-helix occurs along with retraction towards helix D. The long teal dotted line marks the end of random coil for unprotonated LHCII, and the short one for that after acidification. The teal arrow indicates the direction of structural contraction. **g**, Typical bound pigment molecules in the LHCII monomer. The crossing angle between Lut1 and Lut2 (shown as a red arc corner) is defined by two red lines through C-9 to C-15 of Lut1 and C-15 to C-29 of Lut2. **h**, Structural alignment of Lut1–Chl612 pigment pair in the unprotonated structure at pH 7.8 and in the protonated structure at pH 5.4 of the LHCII nanodisc. The dotted lines represent the corresponding interpigment separation, defined as the distance between the Mg atom of Chl612 and the C-15 atom of the conjugated π system of Lut1. **i**, Alignment of the unprotonated structure at pH 7.8 and protonated structure at pH 5.4 of the LHCII nanodisc viewed from the lumenal side. The distance between helix E and D is defined by the distance between the Cα of V96 and G204. The teal arrows indicate the respective motion direction of helix D and E. The yellow arrow points to the specified distance between helix E and D.

we found that T57 forms hydrogen bonds with N61 within each monomer of the protonated conformation (Extended Data Fig. 5d), but these hydrogen bonds do not exist in the unprotonated form. This observation verifies the prediction from a previous molecular dynamics (MD) simulation[27].

At a high pH (7.8), the structures of the LHCII trimer share a common conformation both in detergent solution and in lipid nanodisc, where the protein's secondary structures are consistent with those of the crystal structure. In Fig. 2d, the cryo-EM structure of LHCII in detergent solution at pH 7.8 is superimposed on that of the crystal structure (PDB: 1RWT). The crossing angle between TM helices A and B are different for LHCII in detergent solution and in crystal, which is 119.3° in detergent solution and 117.4° in crystal (Fig. 2d and Extended Data Table 2). The corresponding crossing angles of helices A and B for cryo-EM structures in detergent solution, nanodisc and crystal structures are given in Extended Data Table 2.

At a low pH (5.4), two distinctive classes of 2D images can be identified for LHCII both in detergent solution and in the nanodisc construction. These two classes of images can be fully separated and analysed, resulting in two structures corresponding to different conformations

of LHCII. One of the two conformations can be fully superimposed over the cryo-EM structures from detergent solution and nanodisc at pH 7.8 (Extended Data Fig. 5e), and the two acid sites (D54 and E207) are unprotonated (Fig. 1). The second conformation, however, adopts a different conformational state, with several notable local and protein-wide global changes, including a transition of the 3_{10}-helix E into an α-helix and the formation of a new α-helix segment from the carboxy-terminal (C-terminal) random coil (LHCII nanodisc in Fig. 2e,f and LHCII in detergent solution in Extended Data Fig. 5f,g); in this case, D54 and E207 are protonated.

Compared with the unprotonated structures, we found that helix E of LHCII in nanodisc inserts into the subunit hydrophobic core along with retraction of the C-terminal towards helix D. Interestingly, these secondary structural changes mirror those predicted in MD simulations of LHCII in a lipid membrane under acidic conditions[27–29]. Furthermore, Fourier-transform infrared (FTIR) spectral changes have been detected when going from neutral to acidic conditions in the amide I′ region, corresponding to a change from a 3_{10}-helix and coil to an α-helix conformation (Extended Data Fig. 2c,d). These local conformational changes, involving small segments of α-helix formation at the lumenal side of the membrane, are accompanied by a noticeable change in the crossing angle between helices A and B, from 121.9° (unprotonated structures) to 117.9° (protonated structures) in the nanodisc, and from 119.3° (unprotonated) to 116.6° (protonated) in detergent solution. Because the two types of image at low pH were prepared by increasing the acidity levels of both the detergent solution and nanodisc systems, we hypothesize that the observed coexistence of the unprotonated and protonated conformations of the LHCII trimer are in chemical equilibrium. Also, the fact that a single form of cryo-EM image is obtained at pH 7.8 reaffirms the presence of an equilibrium between two distinctively different conformational states of LHCII. However, the ratio between unprotonated and protonated particles is slightly different for LHCII in detergent solution and in the nanodisc. In particular, we observed that the relative proportion of the protonated conformation increases from 42% in the detergent solution to 71% in the nanodisc. A possible reason for this is that the COO^- groups of aspartic (D) and glutamic (E) acids are more readily protonated in nanodisc than that in solution owing to a more hydrophobic environment. It is known that the pK_a value of aspartic acid can change from 2.4 to 6.4 in different hydrophobic environments[30,31].

We also inspected the conformational changes of Nex in different environments because a twisted Nex conformation has been used as a reporter of the LHCII conformational changes and the energy-quenching state of LHCII[17,24,26]. We found that the configurations of Nex embedded in LHCII in detergent solution (either pH 7.8 or 5.4) and in nanodisc at pH 7.8 are essentially the same as that in the crystal (Extended Data Fig. 5h) with a twisted configuration. Moreover, we noticed that an obvious twist of the hexyl ring of Nex on the stromal side occurs in the protonated structure at pH 5.4, whereas it is absent in the unprotonated structure at pH 7.8 in the nanodisc (Extended Data Fig. 5h).

Lut1–Chl612 separation distance is the key switch

Both ultrafast time-resolved spectroscopic studies[24,32,33] and MD simulations[17,28,32] support excited-state energy transfer (EET) from the lowest excited state (Q_y) of Chl612 to the spectroscopically dark state (S_1) of Lut1 as the main quenching site for LHCII excess energy dissipation. The rate of EET is determined by the electronic coupling between the two locally excited states of Chl612 and Lut1, which is more pronounced on structures at a low pH[27–29,34]. The strength of electronic coupling decays exponentially with the distance between the two chromophores. The fluorescence decay rates measured at conditions corresponding to the present cryo-EM and previous crystal structures of LHCII are plotted in Fig. 3a against the Lut1–Chl612 separation distance. The fluorescence rate is a direct measure of EET from Chl612 to Lut1, and Fig. 3a shows a striking, sharp increase as the Lut1–Chl612 distance becomes shorter than the critical distance of about 5.6 Å. To understand the origin of the observed spectroscopic behaviour, we determined the electronic coupling strength $V_{Q_y^{Chl612},S_1^{Lut1}}$ between the locally excited S_1 state of Lut1 and the Q_y state of Chl612 using multistate density functional theory (MSDFT) on the basis of the four cryo-EM structures determined in this work and the known crystal structures (Extended Data Table 2).

We optimized the locally excited initial state of Chl612 in the presence of Lut1 in its ground state $\Psi_i = |\Phi^{Q_y}_{Chl612}\Phi^{S_0}_{Lut1}\rangle$ (i, initial state) and the locally excited final S_1 state of Lut1 in the presence of Chl612 in the ground state $\Psi_f = |\Phi^{S_0}_{Chl612}\Phi^{S_1}_{Lut1}\rangle$ (f, final state). Then, the electronic coupling matrix element is determined by $V_{Q_y^{Chl612},S_1^{Lut1}} = \langle\Psi_i|\hat{H}|\Psi_f\rangle$, where $\hat{H}$ is the Hamiltonian operator. All calculations were performed using the Minnesota M06-2X density functional and the cc-pVDZ basis set using the Qbics computer program developed in our laboratory. For comparison, we also computed the electronic coupling between Lut1 and the second neighbouring pigment Chl610 (Extended Data Table 2 and Extended Data Fig. 7a). The computed $|V_{Q_y^{Chl612},S_1^{Lut1}}|^2$ values are also given in Fig. 3a and are proportional to fluorescence decay rate. Overall, the contribution from the Lut1-Chl610 pair is much smaller than that of Lut1–Chl612 (Extended Data Table 2), supporting the proposal that the observed fluorescence quenching of Chl612 in LHCII is due to the energy transfer from the Q_y state of Chl612 to the S_1 state of Lut1[24,32,33]. Importantly, Fig. 3a shows that the trends of the experimentally observed fluorescence decay rates and the computed electronic coupling constants are in remarkable agreement. As the two pigments are in close spatial proximity, we used the Dexter model[35] for EET to fit both experimental and computational results, that is, $k_{EET} = k_0 + k^{Lut1}_{Chl612}e^{-\beta(R-R_0)}$, where R is the Lut1–Chl612 separation distance and R_0 is a characteristic contact distance, k^{Lut1}_{Chl612} is the rate constant for the energy transfer from excited Chl612 to Lut1 at a separation of R_0, β is the attenuation factor, and k_0 is a constant accounting for background contributions from all other pigments, independent of the distance between Chl612 and Lut1. We obtained the following values for the rate equation: $k_0 = 0.31\ ns^{-1}$, $k^{Lut1}_{Chl612} = 0.31\ ns^{-1}$, $\beta = 25.0\ Å^{-1}$ and $R_0 = 5.6$ Å.

Several observations can be made. First, the experimental fluorescence decay rates are in good accord with the computed coupling strength for EET from the lowest energy Q_y state of Chl612 to the spectroscopic dark state S_1 of Lut1. The energy in the Lut1 excited state is then dissipated thermally through vibronic coupling, which is not investigated further here. The electronic coupling between Chl610 and Lut1 is much smaller than that of Lut1–Chl612. Therefore, we conclude that the observed variation in fluorescence decay rate is chiefly due to the structural displacement between Lut1 and Chl612 chromophores, which is primarily responsible for the light-harvesting state and excited energy-quenching state transition in LHCII.

Second, carotenoid Lut1 and Lut2 are embedded along the TM helices A and B, respectively (Fig. 2g), and their structure variations and proximity to other pigments, including chlorophylls, are directly associated with the motions of the two helices, with a nearly perfect correlation in their crossing angles (Fig. 3b). Thus, in going from an open conformation (greater crossing angle of the TM helices) to a closed conformation (smaller crossing angle), the antenna pigments Lut1 and Chl612 can be brought closer together with a shorter contact distance. However, Fig. 3c reveals that additional factors are involved. As the pH lowers from 7.8 to 5.4, the interhelical angles between TM helices A and B are decreased by about 2.7° in detergent solution, whereas the corresponding change in the nanodisc is greater, reducing by 4.0°. However, we did not find an obvious change in the distance between Lut1 and Chl612, suggesting that the chlorophyll pigments also undergo dynamic fluctuations to avoid close contact. While Fig. 2h and Extended Data Table 2 show that the Lut1–Chl612 distance

https://doi.org/10.1038/s41477-023-01500-2

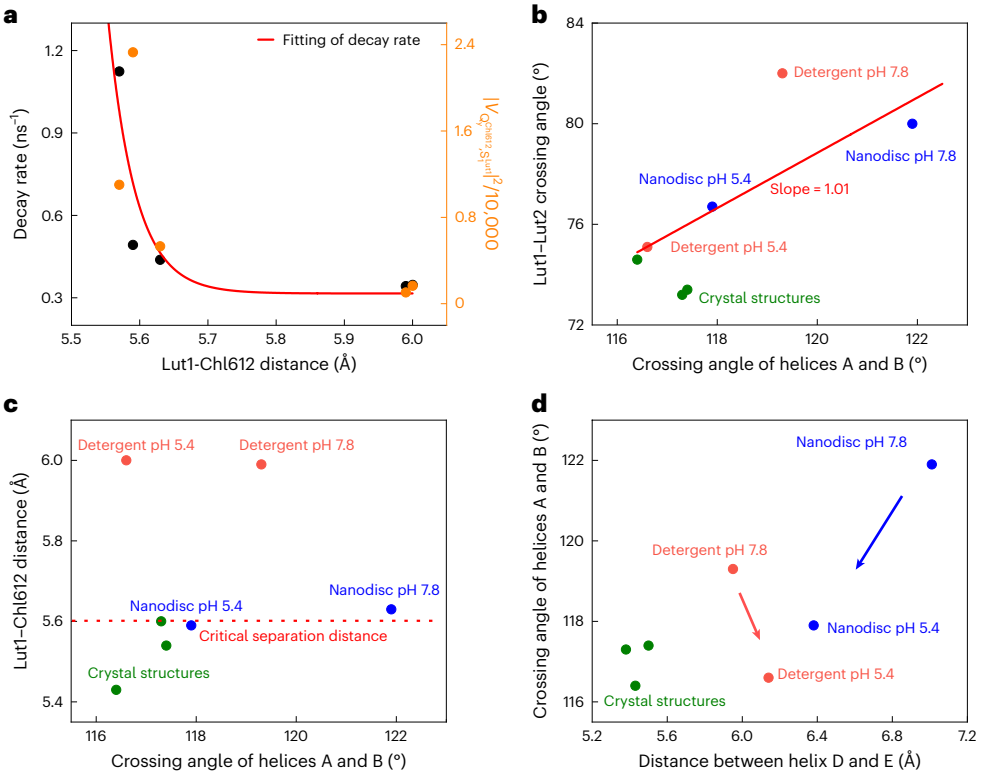

Fig. 3 | Relationships of key structural factors related to state transitions. **a**, The relationship between fluorescence decay rate ($k = 1$/fluorescence lifetime, black circles), Lut1–Chl612 electronic coupling strength $|V_{Q_y\,\mathrm{Chl612},S_1\,\mathrm{Lut1}}|^2/10,000$ (orange circles) against Lut1–Chl612 separation distance (R) and the fitting equation is $k = 0.31 + 0.31 \times 10^{-25(R-5.6)}$ (the fitted line is in red). **b**, Correlation of the crossing angle of the TM helices A and B with that of carotenoid Lut1–Lut2 in different structures. The linear fitting is shown by the red line. **c**, Plot of Lut1–Chl612 distance versus the crossing angle of TM helices A and B in different LHCII structures. The red dotted line marks the critical separation distance of 5.6 Å. **d**, Plot of the distance between helix D and E (defined by Cα of V96 and G204) against the crossing angles of TM helices A and B in different LHCII structures. The blue arrow indicates an increased acidity-induced inward motion of helices D and E as specified in LHCII nanodisc; the red arrow indicates an outward motion of helices D and E in detergent solubilized LHCII after acidification. In **b**–**d**, the green circles represent data from crystal structures (PDB: 1RWT, 2BHW).

is in fact markedly shorter by about 0.4 Å in the nanodisc structures (5.63 Å and 5.59 Å at pH 7.8 and 5.4, respectively) than that in detergent solution (5.99 Å and 6.00 Å at pH 7.8 and 5.4, respectively). In fact, the interpigment distances between Chl612 and Lut1 in the nanodisc structures are similar to those found in the crystal. We attribute the observation of closer contacts between Chl612 and Lut1 to lattice packing in the crystal structures and the structural confinement in the nanodisc environment. A similar outcome can also result from an isolated LHCII confined in rigid media such as gels[36,37] in which the fluorescence lifetime is reduced. Although the variation in the Lut1–Chl612 distance between two atomic distances (5.63 Å and 5.59 Å) in the nanodisc at different pH conditions is rather small, beyond the precision of the structural resolution, structural differences between the two chromophores can be observed in their structural alignment in Fig. 2h. Specifically, the polyene chains of the Lut1 molecule seen in the structures at different pH values are almost perfectly superimposed, but the chlorin ring of Chl612 in the protonated state of LHCII in the nanodisc is visibly closer to Lut1 than that in the unprotonated state. This distance change is consistent with the experimental observation that acid has induced extra fluorescence quenching in LHCII nanodisc (Extended Data Fig. 2a). This small separation difference can have a substantial effect in the computed electronic coupling strength because it occurs right at the critical value of the characteristic distance from the rate equation. The fitted curve of the computed electronic coupling strength (Fig. 3a) shows that a small change in the Lut1–Chl612 distance, for example, 0.02 Å around $R_0 = 5.6$ Å, can result in a transition from a light-harvesting state to energy-quenching state. Figure 3a shows that the fluorescence decay rate is substantially greater at distances shorter than this critical value. When the distance between Chl612 and Lut1 is above R_0, LHCII adopts a light-harvesting state with a slow background fluorescence decay rate at k_0.

Inward motion of helix D and E enhances quenching

What structural changes are responsible for allosterically driving the light-harvesting state to the energy-quenching state transition in energy dissipation? By examining the three crystal structures and the two cryo-EM conformations in nanodisc, we found that the interhelical angle between TM helices A and B is directly correlated with the distance between the local helices D and E (Fig. 3d and Extended Data Table 2). Short distances between helices D and E in crystal structures have been noted and attributed to crowding effects at the trimer–trimer interface, giving rise to van der Waals repulsions between hydrophobic residues of the adjacent trimers[23]. A noticeable decrease in the distance between helices D and E is also observed from 7.01 Å to 6.38 Å as the pH changes from 7.8 to 5.4 in LHCII nanodisc (Fig. 2i), whereas this distance increases slightly for LHCII in detergent solution when the pH is lowered from 7.8 to 5.4. In this case, the cryo-EM structures show that a low-pH environmental condition can induce the formation of two local α-helices, one from the 3_{10}-helix E and one from the C-terminal coil. As a remarkable confirmation of the cryo-EM experiments, these structural transitions have been predicted from molecular dynamic simulations[28]. These local helical structure formations, due to variation in external conditions, cause the allosteric conformation transition of LHCII from

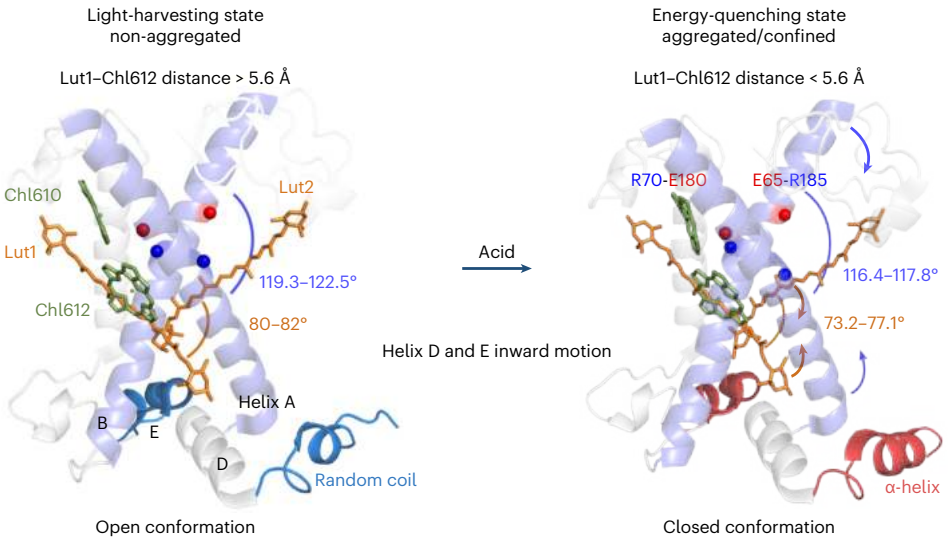

Fig. 4 | Key structural factors that drive state transition. The red circles represent the negatively charged residues, the blue circles represent the positively charged residues, and the curved arrows show the motion of the TM helices A and B and the Lut1–Lut2 pair.

an open form to a closed configuration, characterized by the crossing angle between TM helices A and B. Combining Fig. 3a and Fig. 3d, it can be concluded that it is the inward motion of helices D and E that leads to the reduction in the separation distance between Lut1 and Chl612, switching from a light-harvesting state to an energy-quenching state. However, a global conformational change to the closed conformation does not directly produce the energy-quenching state characterized by a Lut1–Chl612 distance shorter than 5.6 Å, unless LHCII is confined as observed in crystal structures and in the nanodisc at low pH value, consistent with PsbS-assisted aggregation of LHCII in plants. Indeed, in detergent solution, although the TM interhelical angle is changed, albeit to a smaller angle, the distance between Lut1 and Chl612 is not affected. Therefore, a larger lateral constraint force is needed to lead to a shorter Lut1–Chl612 separation distance, hence a shorter fluorescence lifetime. This is verified by inspecting the reported data[38–40] and our current data plotted in Extended Data Fig. 7c. We find that LHCII embedded in a smaller-sized nanodisc induces a shorter fluorescence lifetime. We attribute this observation to a smaller radius of the polypeptide ring, which would give rise to a larger lateral constraint force[41] as the curvature force[42]. This phenomenon has been noted recently and it was concluded that the increased quenching in a smaller-sized nanodisc is due to interactions at the edge of the nanodisc between LHCII and the scaffolding proteins or water molecules[39,43]. Furthermore, recent small angle X-ray scattering measurement of lipid nanodiscs based on membrane scaffold proteins shows that larger nanodiscs are more structurally flexible[44]. This finding is consistent with the present fluorescence lifetime of LHCII nanodiscs of varied size (Extended Data Fig. 7c).

Protein structural changes driving state transition

Our structural findings unambiguously show that it is the combination of the pH-induced secondary protein structural changes and environmental confinement of LHCII that jointly drives the switch between the two functional states of light harvesting and energy quenching. For the NPQ in vivo, in addition to pH variation, the structural protein PsbS in photosystems II and the accumulation of Zea also play important roles in NPQ. PsbS is required for LHCII aggregation after dissociation from the PSII complex as a result of a decreased pH. It has been noted that, without aggregation of LHCII, the lowering of pH is insufficient to induce fluorescence quenching in isolated LHCII[1]. Furthermore, the aggregation of LHCII is inhibited in a PsbS-knockout construct, whereas LHCII aggregation is enhanced when PsbS is overexpressed[45,46]. It has been suggested that PsbS plays a role in maintaining membrane fluidity, triggering the dissociation of PSII–LHCII super-complexes and LHCII aggregation in response to a pH gradient[47,48]. Meanwhile, it has been shown that Zea prompts a rapid NPQ but it also slows down the dark-state recovery kinetics (qE). Consequently, Zea acts as an allosteric regulator rather than a quencher[32,49]. Recently, it has been suggested that, in the presence of unbound Zea, lateral membrane pressure can be increased, which alters protein–lipid interactions and induces conformational changes in LHCII in favour of the energy-quenching state[41,50]. As shown above, either LHCII aggregation or a lateral constraint is a prerequisite for fluorescence quenching. Figure 4 shows the key structural components, highlighting an allosteric mechanism involving a global change of TM helices A and B induced by the formation of two local helices. Specifically, the LHCII trimer acts as a molecular machine: its TM helices A and B constitute the blades of a pair of scissors that pivot around the fulcrum anchored by the salt bridge R70-E180 and E65-R18528 (Extended Data Table 2). The increased acidity induces a local structural transition to convert the 3_{10}-helix E and C-terminal coil into two α-helices at the lumenal side. In LHCII aggregates or a confined state, α-helices D and E are pulled closer together (inward motion) against TM helices A and B, shifting its conformational equilibrium to a smaller crossing angle, and hence a smaller crossing angle of Lut1 and Lut2. The net allosteric effect of such an overall conformation change is to reduce the contact distance between Lut1 and Chl612, enhancing their electronic coupling strength in favour of the excited energy transfer from excited Chls (Q_y) to the S_1 dark state of Lut1. This mechanism also provides a solid structural basis for the various proposed models for the NPQ mechanism, including LHCII aggregation[20,49], change in pigment configuration[51] and an allosteric effect causing protein scissoring motions[23]. The mechanism in Fig. 4 is also consistent with the fact that heat stress can induce aggregation of LHCII both in vivo and in vitro[52]. We further examined the fluorescence reversibility of aggregated LHCII under different pH values by the steady-state fluorescence measurements (Fig. 5) and found that the fluorescence is reversible. Figure 5a shows intensive fluorescence quenching when the β-DDM is lowered from 0.03% to 0.002% (aggregated) at pH 7.8, and extra fluorescence quenching induced by a lower pH value of 5.4 can be observed. Later we restored the pH value for LHCII in 0.002% β-DDM from 5.4 to a neutral condition by the addition of Tris solution, and we observed that the fluorescence intensity increases to 76% of the aggregated LHCII at

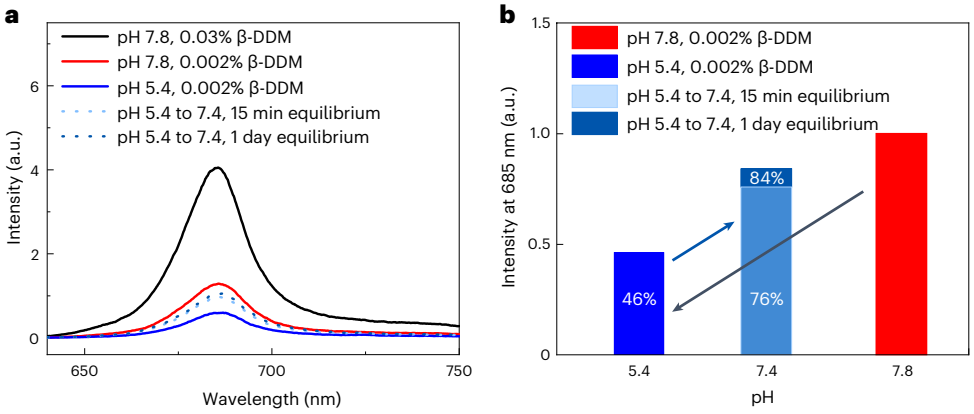

Fig. 5 | Fluorescence spectra indicate the fluorescence reversibility. a, Steady-state fluorescence spectra for LHCII in 0.03% or 0.002% (aggregated) β-DDM at different pH values. Averaged results of three measurements. **b**, Histogram of selected data in **a**, normalized with LHCII in 0.002% β-DDM at pH 7.8. The black arrow shows the fluorescence quenching induced by the lowering of the pH value when LHCII is in an aggregated state; the blue arrow shows the recovery of fluorescence intensity when the pH value is tuned back to neutral.

pH 7.8 after 15 min equilibration, and to 84% after 1 day equilibration (Fig. 5b). The final pH value of 7.4 for the LHCII trimer in 0.002% β-DDM, restored from a pH of 5.4, was measured at the end of the fluorescence measurement.

The fluorescence quenching induced by nanodisc confinement can be related to the xanthophyll cycle and PsbS-dependent NPQ. It has been shown that, in contrast to non-aggregated LHCII, LHCII aggregates showing NPQ have higher mechanical stiffness[53]. In contrast, the membrane under the NPQ condition also becomes more rigid, which is directly related to the xanthophyll cycle[54–56]. Furthermore, single-molecule unfolding experiments showed that inclusion of the non-bilayer lipid monogalactosyldiacylglycerol can substantially increase the mechanical stability (rigidity) of the LHCII trimer in the membrane by exerting lateral pressure on the periphery of LHCII due to steric matching of conically formed monogalactosyldiacylglycerol and the hourglass shape of trimeric LHCII[57]. Thus, we can conclude that the natural photosynthetic systems use both strategies of LHCII aggregation and xanthophyll cycle-dependent lateral pressure on LHCII to maintain a rigid LHCII protein frame and realize efficient NPQ. As a physical model, one confines the LHCII trimer in a lipid nanodisc[32,40] or polyacrylamide gels[37,58] to achieve stiffness in the LHCII structure to mimic the state of aggregated LHCII in Zea-accumulated photosynthetic membrane. Remarkably, obvious fluorescence quenching is observed in these artificial systems[32,38]. Therefore, the LHCII nanodisc bears the same fluorescence-quenching conditions as the xanthophyll cycle and PsbS-dependent NPQ to achieve a rigid state of LHCII. The rigid state of LHCII is a prerequisite for fluorescence quenching. Phenomenologically, rigidity of the LHCII protein is reflected as LHCII in the aggregated state.

In summary, by inspecting a series of LHCII structures spanning from light-harvesting to energy-quenching states, we find that (1) aggregation or confinement of LHCII is a prerequisite for fluorescence quenching, whether LHCII is at high or low pH conditions. The lateral pressure caused by protein aggregation or confinement is a key factor for realizing an energy-quenching state. (2) At low pH conditions, unprotonated and protonated conformations coexist for both LHCII in nanodisc and in detergent solution. In contrast to the unprotonated conformations, the protonated conformation has obvious secondary protein structural changes on the lumenal side, that is, conversion of a 3_{10}-helix E to a normal α-helix, and a C-terminal random coil to a short α-helix. Such conformational changes only lead to enhancement of fluorescence quenching when LHCII is in an aggregated or confined state. (3) The Lut1–Chl612 pigment pair is the main quenching site in LHCII. We found that a slight change in its critical separation distance of 5.6 Å can cause LHCII to switch from a light-harvesting state to an energy-quenching state, and vice versa. This is further corroborated by the calculated electronic coupling strength between the Q_y excited state of Chl612 and the S_1 state of Lut1. The critical distance obtained by the fitting decay rate into a distance-dependent energy transfer equation corresponds to the characteristic contact distance of a Dexter-type energy transfer for the Lut1–Chl612 pigment pair.

Methods

Sample preparation

Preparation of spinach LHCII. LHCII trimers were prepared from spinach leaves according to a previously protocol[28,59], with a few modifications. For purification of trimeric LHCII, thylakoid membrane was washed with an ice-cold buffer containing 50 mM HEPES (pH 7.5), 2 mM $MgCl_2$, 400 mM NaCl and 1 mM EDTA, and subsequently centrifuged at 6,500*g* for 10 min (Avanti JA14; Beckman Coulter). The pellets were solubilized in 5% Triton X-100 to a final protein concentration of 5 mg ml^{-1}, stirred for 15 min in the dark and then centrifuged at 48,000*g* for 25 min (Avanti J-25.5; Beckman Coulter). The PSII-enriched pellets were resuspended in 20 mM Bis-Tris buffer (pH 6.5) and solubilized in 1.25% (w/v) β-DDM. After eliminating the insolubilized material, the solubilized samples were fractionated by ultracentrifugation on a sucrose density gradient at 284,000*g* for 15 h (P40ST rotor; Hitachi), and the continuous gradients containing 0.03% (w/v) β-DDM and 20 mM Bis-Tris (pH 6.5) were prepared in the tube by freezing at −80 °C and thawing at 4 °C. Two major bands of trimeric LHCII and monomeric Lhcb proteins were well separated (Extended Data Fig. 1a), and the trimeric band was harvested with syringes. Centrifugal filters (50 kDa; Amicon Ultra-4-Millipore) were used for sample elution and concentration. LHCII trimers under acidic and mild basic conditions were generated from an addition of Tris-HCl buffer (pH 5.4 and pH 7.8, respectively) to a final concentration of 10 mM, and the non-aggregated LHCII trimers were prepared in 0.03% (w/v) β-DDM.

Expression and purification of membrane scaffold protein MSP1E3D1. The membrane scaffold protein MSP1E3D1 containing 7His-tag was overexpressed and purified following a previously reported protocol[32,60] with minor modifications. The recombinant plasmid, using NcoI and HindIII as restriction sites, was transformed into *Escherichia coli* BL21(DE3) competent cells, and *E. coli* strains were grown in Terrific Broth (TB) medium containing 50 μg ml^{-1} kanamycin with optical density at 600 nm checked every hour. When the optical

density reaches 3.0–4.0, protein production was started by the addition of 1 mM IPTG and the culture was left at 20 °C for about 20 hours. After this induction period, cells were harvested by centrifugation and disrupted promptly using a high-pressure homogenizer at 800 bar pressure. The overexpressed MSP1E3D1 was purified by nickel affinity and size-exclusion chromatography on an AKTA purification system, and the protein purity was checked by running SDS-PAGE (Extended Data Fig. 1b).

Assembly and purification of LHCII nanodisc. The constitution was performed according to the reported protocol[32,40] with a few modifications. LHCII trimer complexes were first mixed with soybean lipids (Sigma) solubilized in 10 mM sodium deoxycholate and 0.1% (w/v) β-DDM and incubated for 1 h at 4 °C on a rotator. The membrane scaffold protein MSP1E3D1 was then added to a final molar ratio of LHCII to lipid to MSP1E3D1 of 1:440:8 and then incubated for 2 h at 4 °C on a rotator. Next, the mixture was eluted with 40 mM Tris-HCl, 125 mM NaCl at a pH of 7.8 using 10 kDa filters (Amicon Ultra-4-Millipore) to remove detergent while self-assembly took place. LHCII nanodiscs were purified through the 6× histidine tag of MSP1E3D1 on a nickel affinity column (HisTrap excel) at 4 °C (Extended Data Fig. 1c), that is, the column was washed with 40 mM Tris-HCl and 125 mM NaCl at a pH of 7.8 and the sample was eluted with 40 mM Tris-HCl, 125 mM NaCl and 500 mM imidazole at a pH of 7.8. Further fast protein liquid chromatography purification was performed on the size-exclusion column (Superdex 200 Increase 10/300 GL; Cytiva) at 4 °C (Extended Data Fig. 1d), and fractions of the main peak were collected and analysed by ultraviolet–visible absorption spectroscopy, SDS-PAGE (Extended Data Fig. 1b) and transmission electron microscopy to identify the peak containing LHCII nanodisc. All measurements were performed within 24 h of sample preparation. For infrared spectroscopy experiments, LHCII nanodiscs were eluted with 40 mM Tris-HCl and 125 mM NaCl in D_2O (99.9%; Cambridge Isotope Laboratories) at pH 7.8 or 5.4.

Cryo-EM data collection and processing. A 3 µl droplet of LHCII nanodisc in a protein concentration of 1.4 mg ml^{-1} was applied to a glow-discharged holey carbon grid (Au, 300 mesh, 1.2 hole size and 1.3 µm spacing; Quantifoil), which was discharged in a mixed atmosphere (O_2 to Ar ratio of 1:3) for 25 s, and LHCII in detergent solution with a protein concentration of 5 mg ml^{-1} was applied to a holey carbon grid (300 mesh, 1.2 µm hole size and 1.3 µm spacing; GIG), which was discharged in a mixed atmosphere (O_2 to Ar ratio of 1:2) for 10 s. The grids were immediately plunge frozen into liquid ethane using Vitrobot Mark IV (FEI) with a 4 s waiting time, a 4 s blotting time and a force level of 2 at 100% humidity and a temperature of 20 °C. Micrographs were collected on a 300 kV FEI Titan Krios electron microscope equipped with a Gatan K3 Summit direct electron detector using beam-image shift data collection methods[61] and a 200 kV Arctica with a Ceta camera was used for sample screening.

The physical pixel size was set to 1.10 Å and 1.04 Å for LHCII nanodisc, and 1.07 Å for LHCII in detergent solution, corresponding to a super-resolution pixel size of 0.55 Å, 0.52 Å and 0.535 Å, respectively, with different Titan Krios machines. For LHCII nanodisc and LHCII in detergent solution, each video was exposed for about 4.5 s and dose fractioned into 32 frames, with a total dose of ~60 e^- $Å^{-2}$, and the defocus values used during data collection varied from −1.5 µm to −2.5 µm. All images were collected using the EPU/SerialEM automated data collection software package[62]. A total of 8,894 micrographs at pH 7.8 and 11,375 micrographs at pH 5.4 were collected for the 3D reconstruction for LHCII nanodisc; 7,282 micrographs at pH 7.8 and 12,453 micrographs at pH 5.4 were collected for LHCII in detergent solution.

All images and particles were processed in the cryoSPARC[63] platform. The images were first motion corrected by 'Patch Motion Correction', and their contrast transfer functions were estimated by 'Patch CTF Estimation (multi)'. The particles were auto-picked using 'Template Picker' and extracted with a box size of 200 pixels. For LHCII nanodisc at pH 7.8, the auto-picked particles (5,123,887) were screened from 8,894 motion-corrected images and selected by 'Reference-Free 2D Classification', while the classes with resolutions below 5 Å were deleted. The remaining particles (817,473) were then used for 'Ab-initio Reconstruction' without imposing any symmetry, and the initial density map was used for 'Homogeneous Refinement' to get a more complete density map with C_1 symmetry. The final density map for LHCII nanodisc at pH 7.8 was obtained at a resolution 2.64 Å by means of 'Non-uniform 3D Refinement' and 'Local Refinement' tools with the 0.143 criterion in the gold-standard Fourier shell correlation coefficient.

The data for LHCII nanodisc at pH 5.4 were processed in a similar manner. The auto-picked particles (6,256,638) from 11,375 motion-corrected images were further screened and selected in the Reference-Free 2D Classification step. A total of 1,214,050 good particles were used for creating a 'clearer' density map by Ab-initio Reconstruction and Homogeneous Refinement. However, these particles were then used for further classification by '3D Classification' for two classes. Two set of particles (860,690 and 353,360) were then left for final Non-uniform 3D Refinement and Local Refinement. Based on the 0.143 criterion in the gold-standard Fourier shell correlation coefficient, the density maps for LHCII nanodisc at pH 5.4 were finally obtained at resolution of 2.63 Å and 2.80 Å, respectively. In addition, the local resolution of the final density maps for the different reconstructions were analysed and estimated by the 'Local Resolution Estimation' in CryoSPARC, using 0.143 as the threshold value. Furthermore, to analyse the accuracy of the critical local structures and to assess the structure's fitness to the density map, we calculated the local resolutions of major pigments and local structures, and the correlation coefficient between the local clusters and map, using phenix.validation_cryoem (Extended Data Fig. 6d).

The data for LHCII in detergent solution at pH 7.8 and 5.4 were processed in the same manner described above.

The homologous cryo-EM structure of LHCII trimer (PDB: 1RWT)[11] was manually fitted into the corresponding maps at different conformations using CHIMERA[64]. Further improvement of the initial models was processed by iterative positional and B-factor refinement using Phenix real space refinement[65]. The final models were corrected and rebuilt in COOT[65], and then evaluated by Phenix Validation cryo-EM and EMRinger[66]. The buried surface area and the root mean square deviation were analysed using PDBePISA (http://pdbe.org/pisa/) and CHIMERA, respectively. The amino acid sequences of LHCII trimer were aligned using ClustalW2 (ref. 67) and visualized with the ENDscript 3 server (http://espript.ibcp.fr)[68]. Figures were made using UCSF Chimera and Pymol (https://www.pymol.org).

Steady and transient fluorescence spectroscopy at room temperature. Steady-state fluorescence spectra of LHCII trimer were measured on an F-7000 spectrometer (Hitachi) at a protein concentration of 0.05 mg ml^{-1} (optical density at 675 nm of 0.36 with 2 mm path length) in a quartz cuvette of 2 mm in optical path length. Time-resolved fluorescence spectra of LHCII in detergent solution and LHCII nanodisc under various conditions were collected using a comprehensive spectroscopy system (Light Conversion, LTU; HARPIA), with a femtosecond laser (PH1-SP-1mJ, Light Conversion, LTU) and an Optical Parametric Amplifier (Light Conversion, LTU; ORPHEUS) as the light source. The excitation wavelength was set to 480 nm with a repetition frequency of 100 kHz at an average power density of 1.5 mW cm^{-2}, and the instrument response factor of the detection system was 0.115 ns. Samples at a protein concentration of 0.03 mg ml^{-1} were placed in a quartz cuvette (JGS1) of 1 mm in optical path length at room temperature. The kinetic decay traces were examined at different excitation powers, which indicates that the decay traces were not affected by the excitation power of 0.5–3.0 mW cm^{-2} under the current conditions.

FTIR spectroscopy at room temperature. FTIR spectra at different pH values were acquired on a spectrometer (VERTEX 70v; Bruker Optics) with a protein concentration of 1.9 mg ml^{-1} and 4.6 mg ml^{-1} for LHCII nanodisc and LHCII in detergent solution, respectively. A three-compartment CaF_2 sample cell with a 50-µm-thick Teflon spacer was used for loading the protein solution and the reference. The measurements were performed in a home-built vacuum chamber, with temperature controlled at 25 °C by a water circulator.

Calculation of the electronic coupling strength between the excited state of Lut1 and Chl612/Chl610. The coordinates of the lutein–chlorophyll pair were extracted from the corresponding experimental structures, where the phytol chain was truncated after the C=C double bond. Constrained geometry optimization was performed at HF/3–21G (HF, Hartree–Fock; 3–21G, 3–21 Gaussian basis set) level using GAUSSIAN16 to relax the hydrogen atoms while all heavy atoms are fixed at the experimental positions. The optimized structures then served as the starting points for electronic coupling calculations with MSDFT. All the MSDFT calculations were performed using the B3LYP functional along with 6–31G(*d*) basis set. First, the singlet excited state of the lutein monomer and chlorophyll monomer were tested to show the reliability of the MSDFT method. It has been proven recently that MSDFT is an exact density functional theory of the excited state, complementing the ubiquitous Kohn–Sham DFT for the ground state, and the method has been used in a number of applications. The ground-state and single excitation configurations constructed in the HOMO-1 to LUMO+1 space are shown in Extended Data Fig. 8a.

The excitation configurations were individually optimized using the TSO[69] method and dynamic correlation were incorporated via DFT. Then, the non-orthogonal state interaction Hamiltonian matrix of these nine configurations could be constructed and solved to obtain the ground and excited states. The off-diagonal element between configurations A and B of the non-orthogonal state interaction Hamiltonian is defined using the overlap-weighted approximation:

$$H_{AB} = \langle \Psi_A | \hat{H} | \Psi_A \rangle + \frac{1}{2} S_{AB} (E_c[\rho_A] + E_c[\rho_B]) \quad (1)$$

where S_{AB} is the overlap integral between the two non-orthogonal Kohn–Sham determinants A and B, $E_c[\rho_A]$ and $E_c[\rho_B]$ are the correlation energies for the determinants A and B, which can be approximated by the energy difference between block-localized DFT and HF theory using block-localized Kohn–Sham (BLKS) orbitals. The excitation energies and corresponding reference values[70,71] are listed in Extended Data Fig. 8b.

The S_1 states for chlorophyll and lutein monomer are $\Phi_{Chl}^{S_1}$ and $\Phi_{Lut}^{S_1}$, respectively. For the Lut–Chl pair, the diabatic states of electronic localized excitation were constructed via BLKS orbitals combined with localization using TSO:

$$\Phi(S_{Lut}) = \hat{A}\{\Psi_{Lut}^{S_1} \Psi_{Chl}^{S_0}\} \quad (2)$$

$$\Phi(S_{Chl}) = \hat{A}\{\Psi_{Lut}^{S_0} \Psi_{Chl}^{S_1}\} \quad (3)$$

where $\hat{A}\{\Psi_{Lut}^{S_1} \Psi_{Chl}^{S_0}\}$ specifies an antisymmetric wave function for the locally excited monomer lutein, coupled with monomer chlorophyll in the ground state, whereas $\hat{A}\{\Psi_{Lut}^{S_0} \Psi_{Chl}^{S_1}\}$ is an antisymmetric wave function for excited monomer chlorophyll, coupled with monomer lutein in the ground state. The locally excited monomer $\Psi_{Lut}^{S_1}$ and $\Psi_{Chl}^{S_1}$ in the Lut–Chl pair were constructed in the same way as $\Phi_{Lut}^{S_1}$ and $\Phi_{Chl}^{S_1}$, illustrated in Extended Data Fig. 8a.

Then, the coupling energy was obtained by solving 2 × 2 the non-orthogonal block-localized DFT Hamiltonian matrix of the two diabatic states:

$$V_{AB} = H_{AB} - S_{AB}\varepsilon_g \quad (4)$$

ε_g is the adiabatic ground-state energy obtained as the lowest eigenvalue by diagonalizing the 2 × 2 Hamiltonian matrix.

More in-depth description of MSDFT theory and calculation can be found in refs. 72–74.

Reporting summary

Further information on research design is available in the Nature Portfolio Reporting Summary linked to this article.

Data availability

The cryo-EM maps of spinach LHCII in nanodisc and in detergent solution at pH 7.8 or pH 5.4 have been deposited in the Electron Microscopy Data Bank under the accession codes EMD-35785, EMD-35786, EMD-35787, EMD-35782, EMD-35783 and EMD-35784. The corresponding structure models are deposited in the Protein Data Bank (PDB) under accession codes 8IX0, 8IX1, 8IX2, 8IWX, 8IWY and 8IWZ. The LHCII crystal structures used in this article can be accessed in the PDB using the accession codes 1RWT and 2BHW.

References

1. Nicol, L., Nawrocki, W. J. & Croce, R. Disentangling the sites of non-photochemical quenching in vascular plants. *Nat. Plants* **5**, 1177–1183 (2019).
2. Demmig-Adams, B., Garab, G., Adams, W. III & Govindjee (eds) *Non-Photochemical Quenching and Energy Dissipation in Plants, Algae and Cyanobacteria* (Springer, 2014).
3. Horton, P., Ruban, A. V. & Walters, R. G. Regulation of light harvesting in green algae. *Annu. Rev. Plant Physiol. Plant Mol. Biol.* **47**, 655–684 (1996).
4. Ruban, A. V. Light harvesting control in plants. *FEBS Lett.* **592**, 3030–3039 (2018).
5. Li, X. P. et al. Regulation of photosynthetic light harvesting involves intrathylakoid lumen pH sensing by the PsbS protein. *J. Biol. Chem.* **279**, 22866–22874 (2004).
6. Ruban, A. V. & Wilson, S. The mechanism of non-photochemical quenching in plants: localization and driving forces. *Plant Cell Physiol.* **62**, 1063–1072 (2021).
7. Murchie, E. H. & Niyogi, K. K. Manipulation of photoprotection to improve plant photosynthesis. *Plant Physiol.* **155**, 86–92 (2011).
8. Dall'Osto, L. et al. Two mechanisms for dissipation of excess light in monomeric and trimeric light-harvesting complexes. *Nat. Plants* **3**, 17033 (2017).
9. De Souza, A. P. et al. Soybean photosynthesis and crop yield are improved by accelerating recovery from photoprotection. *Science* **377**, 851–854 (2022).
10. Kromdijk, J. et al. Improving photosynthesis and crop productivity by accelerating recovery from photoprotection. *Science* **354**, 857–861 (2016).
11. Liu, Z. et al. Crystal structure of spinach major light-harvesting complex at 2.72 Å resolution. *Nature* **428**, 287–292 (2004).
12. Huyer, J. et al. Fluorescence decay kinetics of solubilized pigment protein complexes from the distal, proximal, and core antenna of photosystem II in the range of 10-277 K and absence or presence of sucrose. *J. Phys. Chem. B* **108**, 3326–3334 (2004).
13. Palacios, M. A., de Weerd, F. L., Ihalainen, J. A., van Grondelle, R. & van Amerongen, H. Superradiance and exciton (de) localization in light-harvesting complex II from green plants? *J. Phys. Chem. B* **106**, 5782–5787 (2002).

14. Moya, I., Silvestri, M., Vallon, O., Cinque, G. & Bassi, R. Time-resolved fluorescence analysis of the photosystem II antenna proteins in detergent micelles and liposomes. *Biochemistry* **40**, 12552–12561 (2001).
15. van Oort, B., van Hoek, A., Ruban, A. V. & van Amerongen, H. Aggregation of light-harvesting complex II leads to formation of efficient excitation energy traps in monomeric and trimeric complexes. *FEBS Lett.* **581**, 3528–3532 (2007).
16. Vasil'ev, S. et al. Quenching of chlorophyll a fluorescence in the aggregates of LHCII: steady state fluorescence and picosecond relaxation kinetics. *Biochemistry* **36**, 7503–7512 (1997).
17. Liguori, N., Periole, X., Marrink, S. J. & Croce, R. From light-harvesting to photoprotection: structural basis of the dynamic switch of the major antenna complex of plants (LHCII). *Sci. Rep.* **5**, 15661 (2015).
18. Van Oort, B. et al. Different crystal morphologies lead to slightly different conformations of light-harvesting complex II as monitored by variations of the intrinsic fluorescence lifetime. *Phys. Chem. Chem. Phys.* **13**, 12614–12622 (2011).
19. Barros, T., Royant, A., Standfuss, J., Dreuw, A. & Kuhlbrandt, W. Crystal structure of plant light-harvesting complex shows the active, energy-transmitting state. *EMBO J.* **28**, 298–306 (2009).
20. Horton, P. et al. Control of the light-harvesting function of chloroplast membranes by aggregation of the LHCII chlorophyll–protein complex. *FEBS Lett.* **292**, 1–4 (1991).
21. Tutkus, M., Chmeliov, J., Rutkauskas, D., Ruban, A. V. & Valkunas, L. Influence of the carotenoid composition on the conformational dynamics of photosynthetic light-harvesting complexes. *J. Phys. Chem. Lett.* **8**, 5898–5906 (2017).
22. Schlau-Cohen, G. S. et al. Single-molecule identification of quenched and unquenched states of LHCII. *J. Phys. Chem. Lett.* **6**, 860–867 (2015).
23. Yan, H., Zhang, P., Wang, C., Liu, Z. & Chang, W. Two lutein molecules in LHCII have different conformations and functions: insights into the molecular mechanism of thermal dissipation in plants. *Biochem. Biophys. Res. Commun.* **355**, 457–463 (2007).
24. Ruban, A. V. et al. Identification of a mechanism of photoprotective energy dissipation in higher plants. *Nature* **450**, 575–578 (2007).
25. Standfuss, J., Terwisscha van Scheltinga, A. C. T., Lamborghini, M. & Kühlbrandt, W. Mechanisms of photoprotection and nonphotochemical quenching in pea light-harvesting complex at 2.5 A resolution. *EMBO J.* **24**, 919–928 (2005).
26. Pascal, A. A. et al. Molecular basis of photoprotection and control of photosynthetic light-harvesting. *Nature* **436**, 134–137 (2005).
27. Daskalakis, V. et al. Structural basis for allosteric regulation in the major antenna trimer of photosystem II. *J. Phys. Chem. B* **123**, 9609–9615 (2019).
28. Li, H. et al. Dynamical and allosteric regulation of photoprotection in light harvesting complex II. *Sci. China Chem.* **63**, 1121–1133 (2020).
29. Daskalakis, V., Papadatos, S. & Stergiannakos, T. The conformational phase space of the photoprotective switch in the major light harvesting complex II. *Chem. Commun.* **56**, 11215–11218 (2020).
30. Navakoudis, E., Stergiannakos, T. & Daskalakis, V. A perspective on the major light-harvesting complex dynamics under the effect of pH, salts, and the photoprotective PsbS protein. *Photosynth. Res.* **156**, 163–177 (2022).
31. Ruban, A. V., Johnson, M. P. & Duffy, C. D. The photoprotective molecular switch in the photosystem II antenna. *Biochim. Biophys. Acta* **1817**, 167–181 (2012).
32. Son, M., Pinnola, A., Gordon, S. C., Bassi, R. & Schlau-Cohen, G. S. Observation of dissipative chlorophyll-to-carotenoid energy transfer in light-harvesting complex II in membrane nanodiscs. *Nat. Commun.* **11**, 1295 (2020).
33. Mascoli, V. et al. Capturing the quenching mechanism of light-harvesting complexes of plants by zooming in on the ensemble. *Chemistry* **5**, 2900–2912 (2019).
34. Maity, S., Daskalakis, V., Elstner, M. & Kleinekathofer, U. Multiscale QM/MM molecular dynamics simulations of the trimeric major light-harvesting complex II. *Phys. Chem. Chem. Phys.* **23**, 7407–7417 (2021).
35. Madjet, M. E.-A., Müh, F. & Renger, T. Deciphering the influence of short-range electronic couplings on optical properties of molecular dimers: application to 'special pairs' in photosynthesis. *J. Phys. Chem. B* **113**, 12603–12614 (2009).
36. Saccon, F. et al. A protein environment-modulated energy dissipation channel in LHCII antenna complex. *iScience* **23**, 101430 (2020).
37. Ilioaia, C., Johnson, M. P., Horton, P. & Ruban, A. V. Induction of efficient energy dissipation in the isolated light-harvesting complex of photosystem II in the absence of protein aggregation. *J. Biol. Chem.* **283**, 29505–29512 (2008).
38. Yamano, N., Wang, P., Dong, F. Q. & Zhang, J. P. Lipid-enhanced photoprotection of LHCII in membrane nanodisc by reducing chlorophyll triplet production. *J. Phys. Chem. B* **126**, 2669–2676 (2022).
39. Manna, P. & Schlau-Cohen, G. S. Photoprotective conformational dynamics of photo synthetic light-harvesting proteins. *Biochim. Biophys. Acta Bioenerg.* **1863**, 148543 (2022).
40. Pandit, A. et al. Assembly of the major light-harvesting complex II in lipid nanodiscs. *Biophys. J.* **101**, 2507–2515 (2011).
41. Tietz, S. et al. A proteoliposome-based system reveals how lipids control photosynthetic light harvesting. *J. Biol. Chem.* **295**, 1857–1866 (2020).
42. Van Den Brink-Van Der Laan, E., Antoinette Killian, J. & De Kruijffu, B. Nonbilayer lipids affect peripheral and integral membrane proteins via changes in the lateral pressure profile. *Biochim. Biophys. Acta Biomembr.* **1666**, 275–288 (2004).
43. Manna, P., Davies, T., Hoffmann, M., Johnson, M. P. & Schlau-Cohen, G. S. Membrane-dependent heterogeneity of LHCII characterized using single-molecule spectroscopy. *Biophys. J.* **120**, 3091–3102 (2021).
44. Johansen, N. T. et al. Structural and biophysical properties of supercharged and circularized nanodiscs. *Langmuir* **37**, 6681–6690 (2021).
45. Goral, T. K. et al. Light-harvesting antenna composition controls the macrostructure and dynamics of thylakoid membranes in *Arabidopsis*. *Plant J.* **69**, 289–301 (2012).
46. Nicol, L. & Croce, R. The PsbS protein and low pH are necessary and sufficient to induce quenching in the light-harvesting complex of plants LHCII. *Sci. Rep.* **11**, 7415 (2021).
47. Betterle, N. et al. Light-induced dissociation of an antenna hetero-oligomer is needed for non-photochemical quenching induction. *J. Biol. Chem.* **284**, 15255–15266 (2009).
48. Johnson, M. P. & Ruban, A. V. Restoration of rapidly reversible photoprotective energy dissipation in the absence of PsbS protein by enhanced ΔpH. *J. Biol. Chem.* **286**, 19973–19981 (2011).
49. Horton, P., Wentworth, M. & Ruban, A. V. Control of the light harvesting function of chloroplast membranes: the LHCII-aggregation model for non-photochemical quenching. *FEBS Lett.* **579**, 4201–4206 (2005).
50. Azadi-Chegeni, F. et al. Protein dynamics and lipid affinity of monomeric, zeaxanthin-binding LHCII in thylakoid membranes. *Biophys. J.* **121**, 396–409 (2022).
51. Wentworth, M., Ruban, A. V. & Horton, P. Thermodynamic investigation into the mechanism of the chlorophyll fluorescence quenching in isolated photosystem II light-harvesting complexes. *J. Biol. Chem.* **278**, 21845–21850 (2003).

52. Tang, Y. et al. Heat stress induces aggregation of the light harvesting complex of photosystem II in spinach plants. *Plant Physiol.* **143**, 629–638 (2007).
53. Janik, E. et al. Molecular architecture of plant thylakoids under physiological and light stress conditions: a study of lipid-light-harvesting complex II model membranes. *Plant Cell* **25**, 2155–2170 (2013).
54. Havaux, M. Carotenoids as membrane stabilizers in chloroplasts. *Trends Plant Sci.* **3**, 147–151 (1998).
55. Tardy, F. & Havaux, M. Thylakoid membrane fluidity and thermo-stability during the operation of the xanthophyll cycle in higher-plant chloroplasts. *Biochim. Biophys. Acta* **1330**, 179–193 (1997).
56. Gruszecki, W. I. & Sielewiesiuk, J. Galactolipid multibilayers modified with xanthophylls: orientational and diffractometric studies. *Biochim. Biophys. Acta* **1069**, 21–26 (1991).
57. Seiwert, D., Witt, H., Janshoff, A. & Paulsen, H. The non-bilayer lipid MGDG stabilizes the major light-harvesting complex (LHCII) against unfolding. *Sci. Rep.* **7**, 5158 (2017).
58. Rutkauskas, D., Chmeliov, J., Johnson, M., Ruban, A. & Valkunas, L. Exciton annihilation as a probe of the light-harvesting antenna transition into the photoprotective mode. *Chem. Phys.* **404**, 123–128 (2012).
59. Caffarri, S., Kouril, R., Kereiche, S., Boekema, E. J. & Croce, R. Functional architecture of higher plant photosystem II supercomplexes. *EMBO J.* **28**, 3052–3063 (*2009*).
60. Ritchie, T. et al. Reconstitution of membrane proteins in phospholipid bilayer nanodiscs. *Methods Enzymol.* **464**, 211–231 (2009).
61. Wu, C. L., Huang, X. J., Cheng, J., Zhu, D. J. & Zhang, X. Z. High-quality, high-throughput cryo-electron microscopy data collection via beam tilt and astigmatism-free beam-image shift. *J. Struct. Biol.* **208**, 107396 (2019).
62. Mastronarde, D. N. Automated electron microscope tomography using robust prediction of specimen movements. *J. Struct. Biol.* **152**, 36–51 (2005).
63. Punjani, A., Rubinstein, J. L., Fleet, D. J. & Brubaker, M. A. cryoSPARC: algorithms for rapid unsupervised cryo-EM structure determination. *Nat. Methods* **14**, 290–296 (2017).
64. Pettersen, E. F. et al. UCSF chimera—a visualization system for exploratory research and analysis. *J. Comput. Chem.* **25**, 1605–1612 (2004).
65. Adams, P. D. et al. PHENIX: a comprehensive Python-based system for macromolecular structure solution. *Acta Crystallogr. D* **66**, 213–221 (2010).
66. Emsley, P. & Cowtan, K. Coot: model-building tools for molecular graphics. *Acta Crystallogr. D* **60**, 2126–2132 (2004).
67. Larkin, M. A. et al. Clustal W and Clustal X version 2.0. *Bioinformatics* **23**, 2947–2948 (2007).
68. Robert, X. & Gouet, P. Deciphering key features in protein structures with the new ENDscript server. *Nucleic Acids Res.* **42**, W320–W324 (2014).
69. Grofe, A. et al. Generalization of block-localized wave function for constrained optimization of excited determinants. *J. Chem. Theory Comput.* **17**, 277–289 (2021).
70. Sirohiwal, A., Berraud-Pache, R., Neese, F., Izsak, R. & Pantazis, D. A. Accurate computation of the absorption spectrum of chlorophyll alpha with pair natural orbital coupled cluster methods. *J. Phys. Chem. B* **124**, 8761–8771 (2020).
71. Dreuw, A. Influence of geometry relaxation on the energies of the S1 and S2 states of violaxanthin, zeaxanthin, and lutein. *J. Phys. Chem. A* **110**, 4592–4599 (2006).
72. Zhao, R., Hettich, C. P. & Chen, X. Minimal-active-space multistate density functional theory for excitation energy involving local and charge transfer states. *npj Comput. Mater.* **7**, 148 (2021).
73. Zhao, R. et al. Dynamic-then-static approach for core excitations of open-shell molecules. *J. Phys. Chem. Lett.* **12**, 7409–7417 (2021).
74. Gao, J., Grofe, A., Ren, H. & Bao, P. Beyond Kohn–Sham approximation: hybrid multistate wave function and density functional theory. *J. Phys. Chem. Lett.* **7**, 5143–5149 (2016).

Acknowledgements

We thank the Beijing National Laboratory for Condensed Matter Physics, Institute of Physics, Chinese Academy of Science and Beijing Branch of Songshan Lake Laboratory for Materials Science for our cryo-EM work. We thank the Center for Biological Imaging, Institute of Biophysics, Chinese Academy of Science for our cryo-EM work, and we thank B. Zhu, X. Huang and L. Chen for their help taking EM images. We thank the cryo-EM centre of the Southern University of Science and Technology for our cryo-EM work and we thank L. Fu, J. Wu and S. Xu for their help taking EM images. We thank T. Kuang for encouragement and M. Li for in-depth discussion. We thank H. Yan for sending us the crystal structure data of LHCII from cucumber. This work was supported by the Chinese Academy of Sciences (grant nos. QYZDJ-SSW-SYS017, XDB33000000 and YJKYYQ20170046 to Y. Weng), the National Natural Science Foundation of China (grant no. 11721404 to Y. Weng) and the Shenzhen Municipal Science and Technology Innovation Commission (grant no. KQTD2017-0330155106581 to J.G.).

Author contributions

M.R. and H.L. purified samples and collected cryo-EM data. Y.Z., Z.W., W.D., Yumei Wang and D.S. assisted with data collection. W.D. processed cryo-EM data and reconstructed the density map. M.R., H.L. and Y. Weng analysed the structures. R.Z. and J.Z. wrote the software. R.Z., Yingjie Wang and J.G. calculated and analysed the electronic coupling. H.L. characterized and analysed the fluorescence spectra and lifetime measurement. The article was written by M.R., W.D., J.G. and Y. Weng with contributions by all authors. M.R., H.L., W.D. and Y. Weng prepared all figures. Y. Weng conceived of and coordinated the whole project.

Competing interests

The authors declare no competing interests.

Additional information

Extended data is available for this paper at https://doi.org/10.1038/s41477-023-01500-2.

Supplementary information The online version contains supplementary material available at https://doi.org/10.1038/s41477-023-01500-2.

Correspondence and requests for materials should be addressed to Jiali Gao, Wei Ding or Yuxiang Weng.

Peer review information *Nature Plants* thanks Mei Li and Nicoletta Liguor for their contribution to the peer review of this work.

https://doi.org/10.1038/s41477-023-01500-2

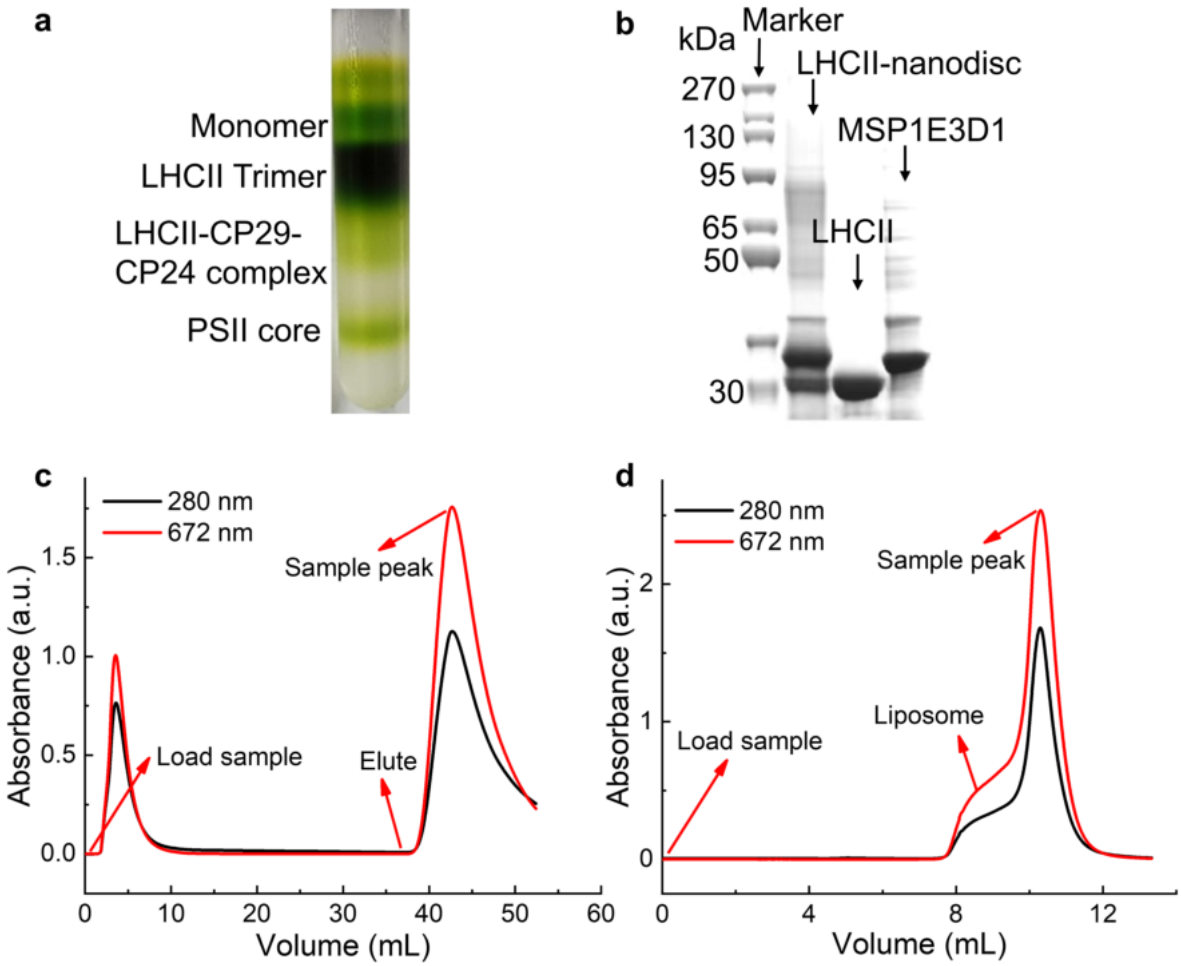

Extended Data Fig. 1 | Sample purification of LHCII and LHCII nanodisc. **a**, Sucrose density gradient ultra-centrifugation separation of LHCII trimer. **b**, SDS-PAGE of LHCII nanodisc, LHCII in detergent solution and membrane scaffold protein MSP1E3D1. The experiment was repeated three times independently with similar results. **c**, Absorption trace at 280 nm and 672 nm during the Ni-NTA column purification of LHCII nanodisc. **d**, Absorption trace at 280 nm and 672 nm during size exclusion chromatography column purification of LHCII nanodisc.

https://doi.org/10.1038/s41477-023-01500-2

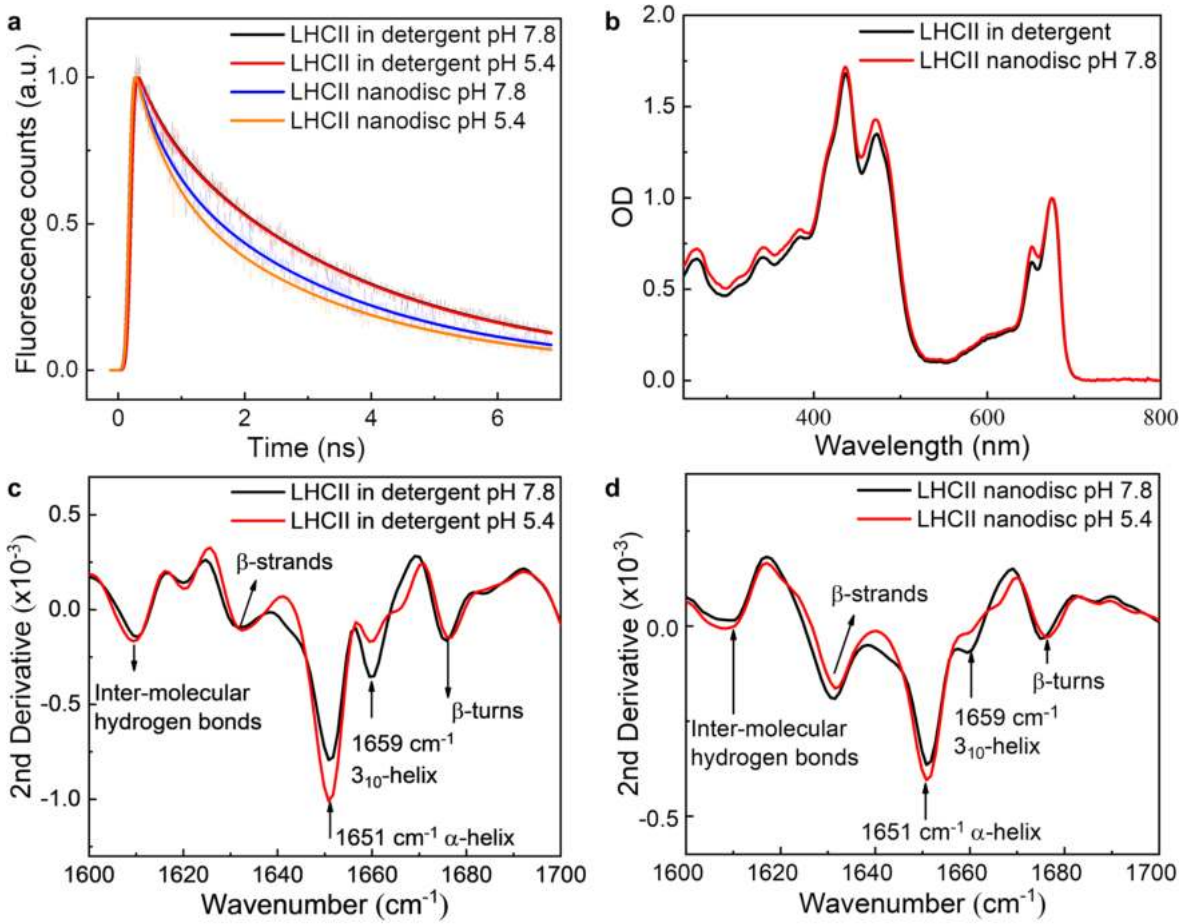

e

LHCII	t_1 (ns)	A_1 (%)	t_2 (ns)	A_2 (%)	t_{avg} (ns)
Detergent pH 7.8	3.42	83%	0.48	17%	2.92
Detergent pH 5.4	3.39	83%	0.45	17%	2.88
Nanodisc pH 7.8	3.05	70%	0.5	30%	2.28
Nanodisc pH 5.4	2.92	63%	0.51	37%	2.03

Extended Data Fig. 2 | Fluorescence decay kinetics and UV-vis and FTIR absorption spectra of LHCII nanodisc and LHCII in detergent solution. All spectra are the averaged results of three measurements. **a**, Fluorescence decay kinetics of LHCII in 0.03% β-DDM at pH 7.8 and 5.4 and LHCII nanodisc at pH 7.8 and 5.4 respectively, excited at 480 nm laser with a repetition frequency of 100 kHz, an average power density of 1.5 mW/cm^2, an instrumental response factor (IRF) of 0.115 ns. **b**, UV-vis absorption spectra of LHCII in detergent solution and LHCII nanodisc. **c**, Secondary derivative FTIR spectra of LHCII trimer in 0.03% DDM at pH 7.8 and 5.4 respectively. **d**, Secondary derivative FTIR spectra of LHCII nanodisc at pH 7.8 and 5.4 respectively. **e**, Lifetime constants and the associated amplitudes of LHCII in different environments based on biexponential fitting.

https://doi.org/10.1038/s41477-023-01500-2

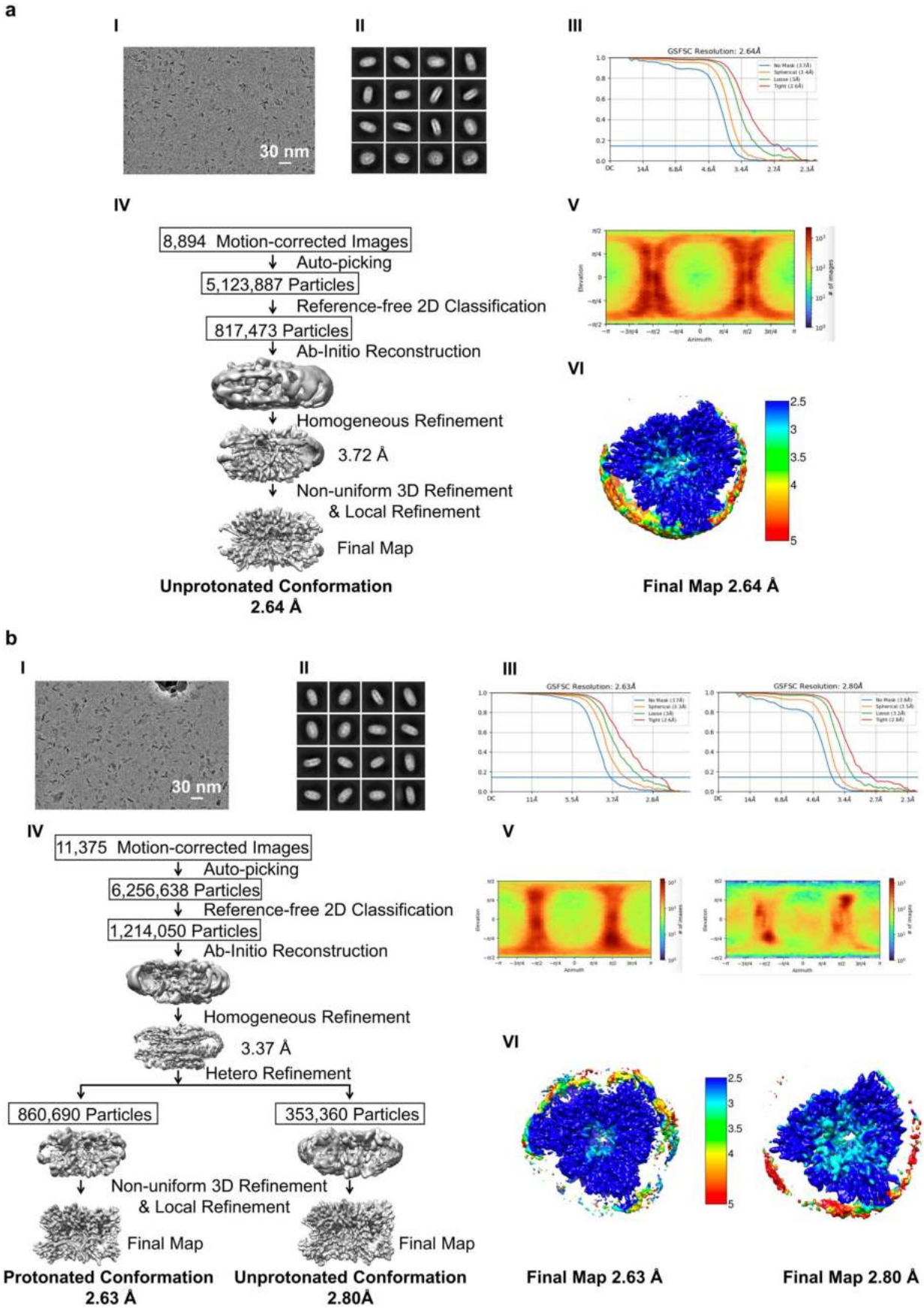

Extended Data Fig. 3 | See next page for caption.

https://doi.org/10.1038/s41477-023-01500-2

Extended Data Fig. 3 | Structural analysis flow chart of LHCII nanodisc at pH 7.8 (a) and 5.4 (b). a, **I**, A representative cryo-EM image of 8,894 collected for LHCII nanodisc at pH 7.8. **II**, 2D class averages of characteristic projection views of cryo-EM particles selected for further processing. **III**, Gold-standard Fourier Shell Correlation (FSC) curves of unprotonated conformation at pH 7.8, the 0.143 cut-off value is indicated by a horizontal blue line. **IV**, Flowchart for cryo-EM data processing. **V**, Angular distribution plot of particles used for final 3D refinement. The distribution was calculated with CryoSPARC 4.0. The different colors indicate the different number of particles that have such orientations according to the bar shown on the right. **VI**, Local resolution map analyzed by the local resolution estimation tool in CryoSPARC. **b**, Protonated (left) and unprotonated (right) conformation at pH 5.4; the detailed illustrations of I, II, III, IV, V and VI are the same as those in **a**.

https://doi.org/10.1038/s41477-023-01500-2

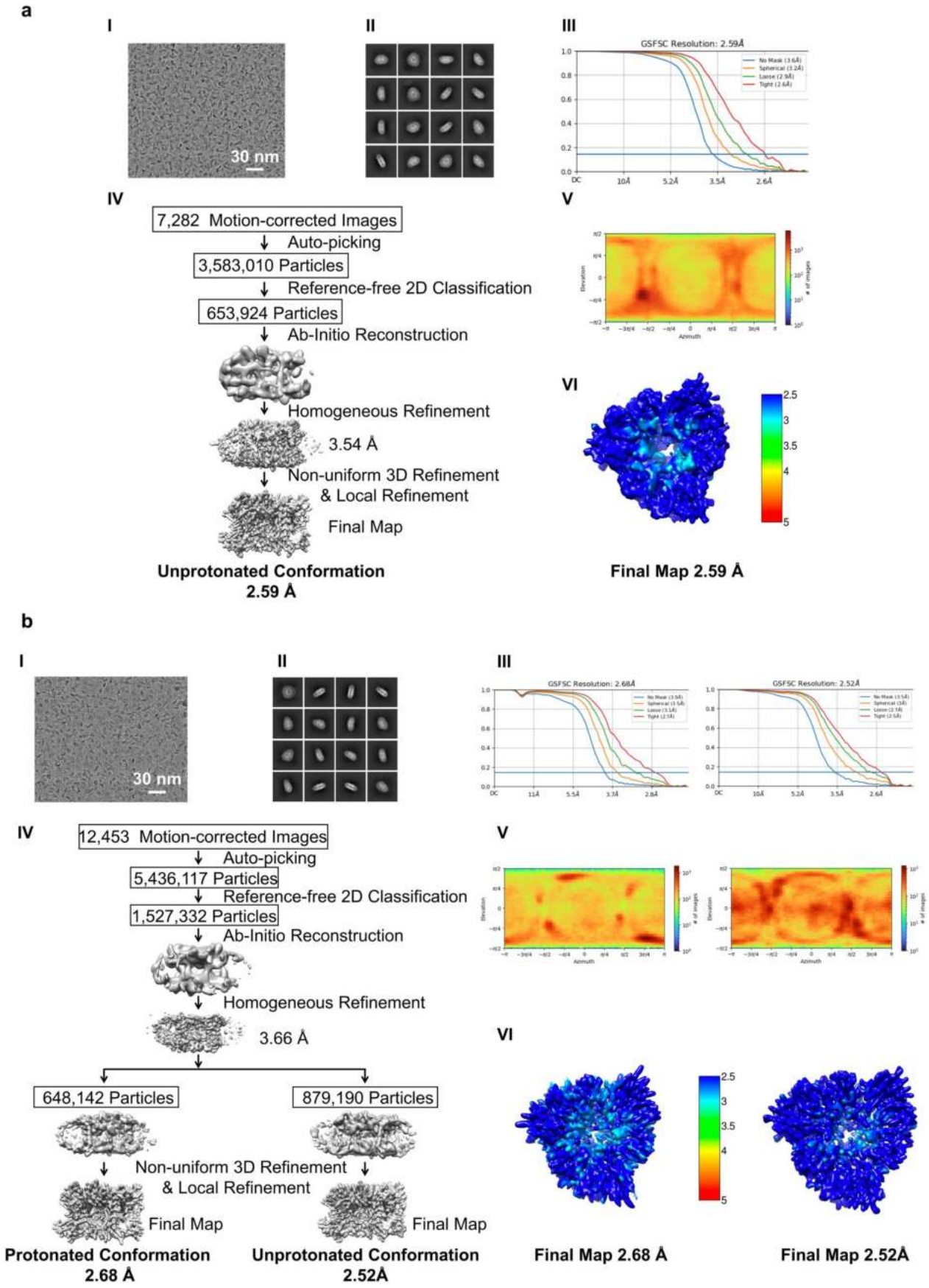

Extended Data Fig. 4 | See next page for caption.

https://doi.org/10.1038/s41477-023-01500-2

Extended Data Fig. 4 | Structural analysis flow chart of LHCII in detergent solution at pH 7.8 (a) and 5.4 (b). a, **I**, A representative cryo-EM image of 7,282 collected for LHCII in detergent solution at pH 7.8. **II**, 2D class averages of characteristic projection views of cryo-EM particles selected for further processing. **III**, Gold-standard Fourier Shell Correlation (FSC) curves of unprotonated conformation at pH 7.8, the 0.143 cut-off value is indicated by a horizontal blue line. **IV**, Flowchart for cryo-EM data processing. **V**, Angular distribution plot of particles used for final 3D refinement. The distribution was calculated with CryoSPARC 4.0. The different colors indicate the different number of particles that have such orientations according to the bar shown on the right. **VI**, Local resolution map analyzed by the local resolution estimation tool in CryoSPARC. **b**, Protonated (left) and unprotonated (right) conformation at pH 5.4; the detailed illustrations of I, II, III, IV, V and VI are the same as those in **a**.

https://doi.org/10.1038/s41477-023-01500-2

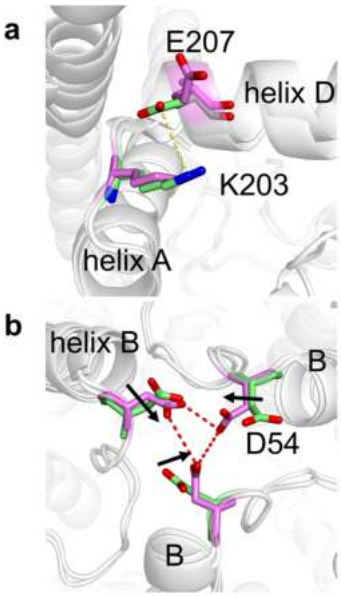

c

Structures	K203-E207	D54-D54[&]
	Average distance (Å)	Average distance (Å)
Detergent pH 7.8	4.04 (0.26)	5.15 (0.68)
Detergent pH 5.4-1[#]	4.10 (0.22)	5.53 (0.49)
Detergent pH 5.4-2[$]	5.39 (0.12)	3.42 (0.68)
Nanodisc pH 7.8	4.01 (0.47)	8.49 (0.76)
Nanodisc pH 5.4-1[#]	3.98 (0.31)	8.71 (0.91)
Nanodisc pH 5.4-2[$]	5.49 (0.05)	4.00 (0.81)

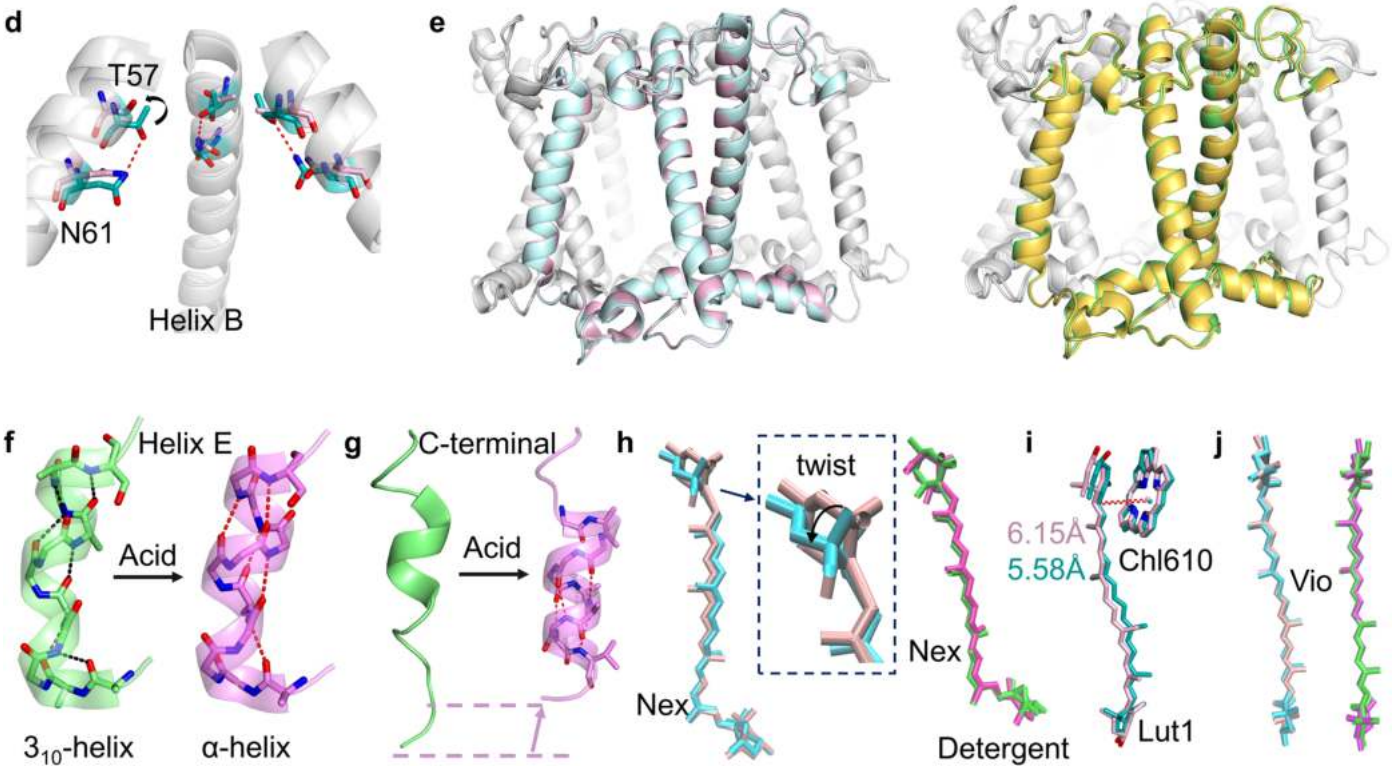

Extended Data Fig. 5 | Comparison of protein secondary structures and pigments in different conformations. a, **b**, Formation or disruption of salt bridge between K203 and E207 (**a**) at lumenal side and hydrogen bonds network among D54 (**b**) at stromal side of each monomer in the unprotonated (green) and protonated (magenta) conformations of LHCII in detergent solution, suggesting the protonation of E207 and D54 in LHCII after acidification. **c**, Average distance for K203-E207 and D54-D54 in different conformations. [&]: D54-D54 between three monomers. [#]: Unprotonated conformation at low pH (5.4) condition. [&]: Protonated conformation at low pH (5.4) condition. Data in bracket are the standard deviations of the average values. **d**, T57 and N61 in unprotonated (pink) and protonated (teal) conformations for LHCII nanodisc, the black arrow indicates the conformational transitions associated with protonation. **e**, Alignment of unprotonated structures at pH 7.8 (pink, green) and pH 5.4 (light blue, yellow) of LHCII in nanodisc (left) and in detergent solution (right). **f**, **g**, Structural comparison for helix E (**f**) and C-terminal (**g**) of LHCII in detergent solution without (pH 7.8, left) and with acidification (pH 5.4, right), a change from 3_{10}-helix or C-terminal random coil to α-helix is observed, along with C-terminal retraction towards helix D. **h**, Nex alignment of unprotonated structure at pH 7.8 (pink; green) and corresponding protonated structure at pH 5.4 (teal; magenta) of LHCII nanodisc (left) and LHCII in detergent solution (right), respectively, and a twist of the hexyl ring at stromal side occurs upon acidification for LHCII in nanodisc (expanded view). **i**, Lut1 and adjacent Chl610 pigment alignments of unprotonated structure at pH 7.8 (pink) and corresponding protonated structure at pH 5.4 (teal) of LHCII nanodisc, Lut1-Chl610 distance is 6.15 Å and 5.58 Å respectively, characterized by the Mg atom of Chl610 and the C_{27} atom in the conjugated π-system of Lut1. **j**, Vio alignment of unprotonated structure at pH 7.8 (pink; green) and corresponding protonated structure at pH 5.4 (teal; magenta) of LHCII in nanodisc (left) and in detergent solution (right).

https://doi.org/10.1038/s41477-023-01500-2

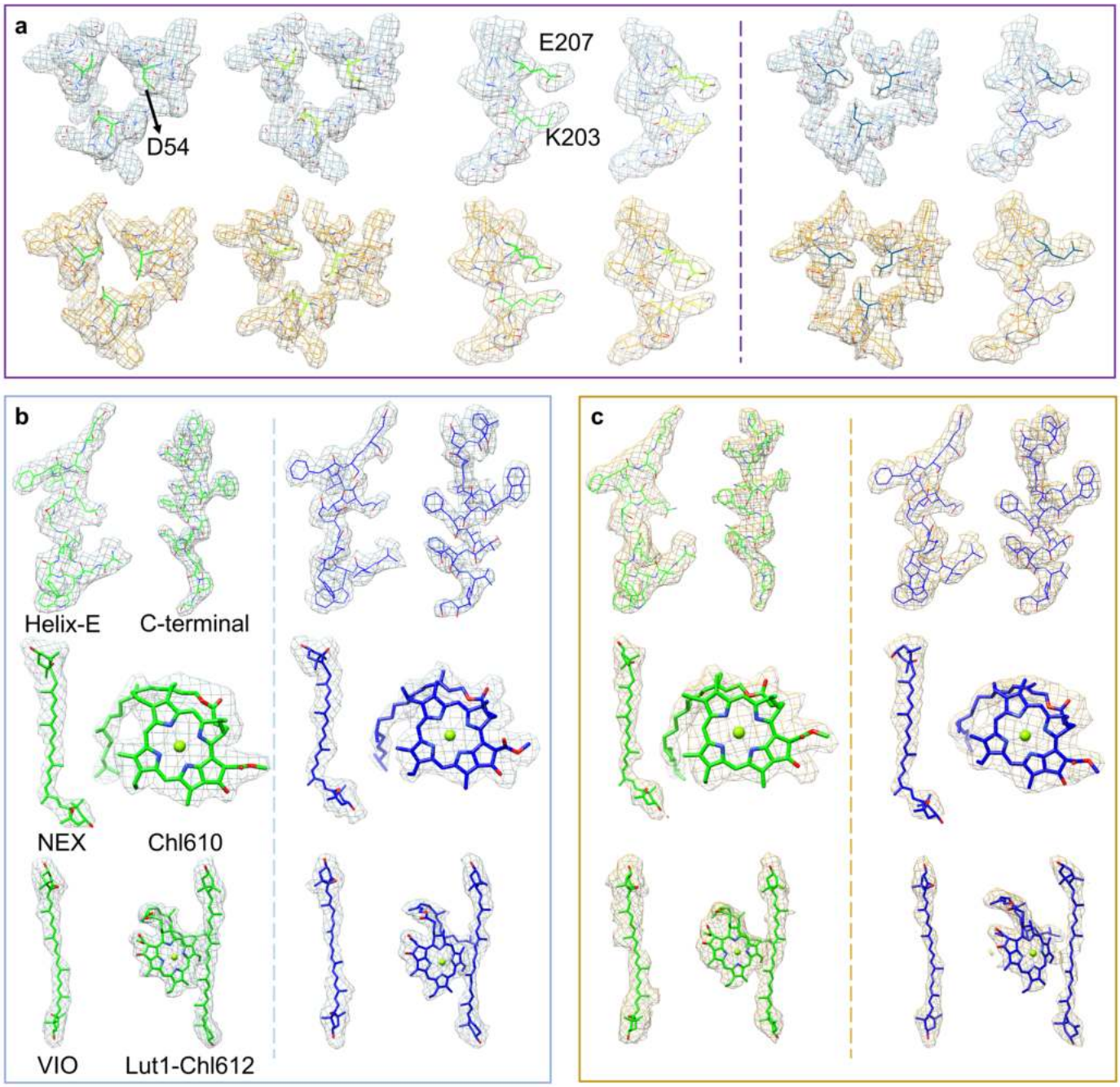

d

Structures	Local resolution (Å)						
	Helix-E	C-terminal	NEX	VIO	Lut1	Chl610	Chl612
Nanodisc pH 7.8	2.58 (0.90)	2.52 (0.88)	2.57 (0.92)	2.65 (0.91)	2.61 (0.92)	2.64 (0.84)	2.54 (0.87)
Nanodisc pH 5.4#	2.40 (0.87)	2.43 (0.87)	2.36 (0.87)	2.48 (0.88)	2.34 (0.89)	2.41 (0.84)	2.47 (0.83)
Detergent pH 7.8	2.52 (0.84)	2.55 (0.85)	2.49 (0.86)	2.74 (0.80)	2.66 (0.81)	2.63 (0.84)	2.48 (0.85)
Detergent pH 5.4#	2.46 (0.87)	2.62 (0.90)	2.55 (0.89)	2.61 (0.88)	2.42 (0.86)	2.51 (0.87)	2.52 (0.89)

Extended Data Fig. 6 | See next page for caption.

https://doi.org/10.1038/s41477-023-01500-2

Extended Data Fig. 6 | Electron-density map and resolution of local structures and pigments of unprotonated structures at pH 7.8 and protonated structures at pH 5.4 for LHCII in nanodisc and in detergent solution respectively. Local structure of pigments is double checked in COOT with best real space refinement statistics, such as Bonds, Angles, Torsions, Planes, Chirals, Non-bonded and Rama Plot. **a**, Local structural density map that involved D54-D54 and K203-E207 for LHCII in nanodisc (upper panel) and in detergent solution (lower panel), unprotonated structures are to the left of the dashed line (the key residues are shown in green (pH 7.8) or yellow (pH 5.4)) and protonated structures are at right (key residues are shown in blue). **b**, Density map of local structures and pigments for the unprotonated conformation at pH 7.8 (left) and protonated conformation at pH 5.4 (right) of LHCII in nanodisc. **c**, Density map of local structures and pigments for the unprotonated conformation at pH 7.8 (left) and protonated conformation at pH 5.4 (right) of LHCII in detergent solution. **d**, Local resolution and local correlation coefficients (in bracket, model vs map) for significant structures in different LHCII conformations, analyzed by phenix.validation_cryoem. [#]: Protonated conformation at pH 5.4.

https://doi.org/10.1038/s41477-023-01500-2

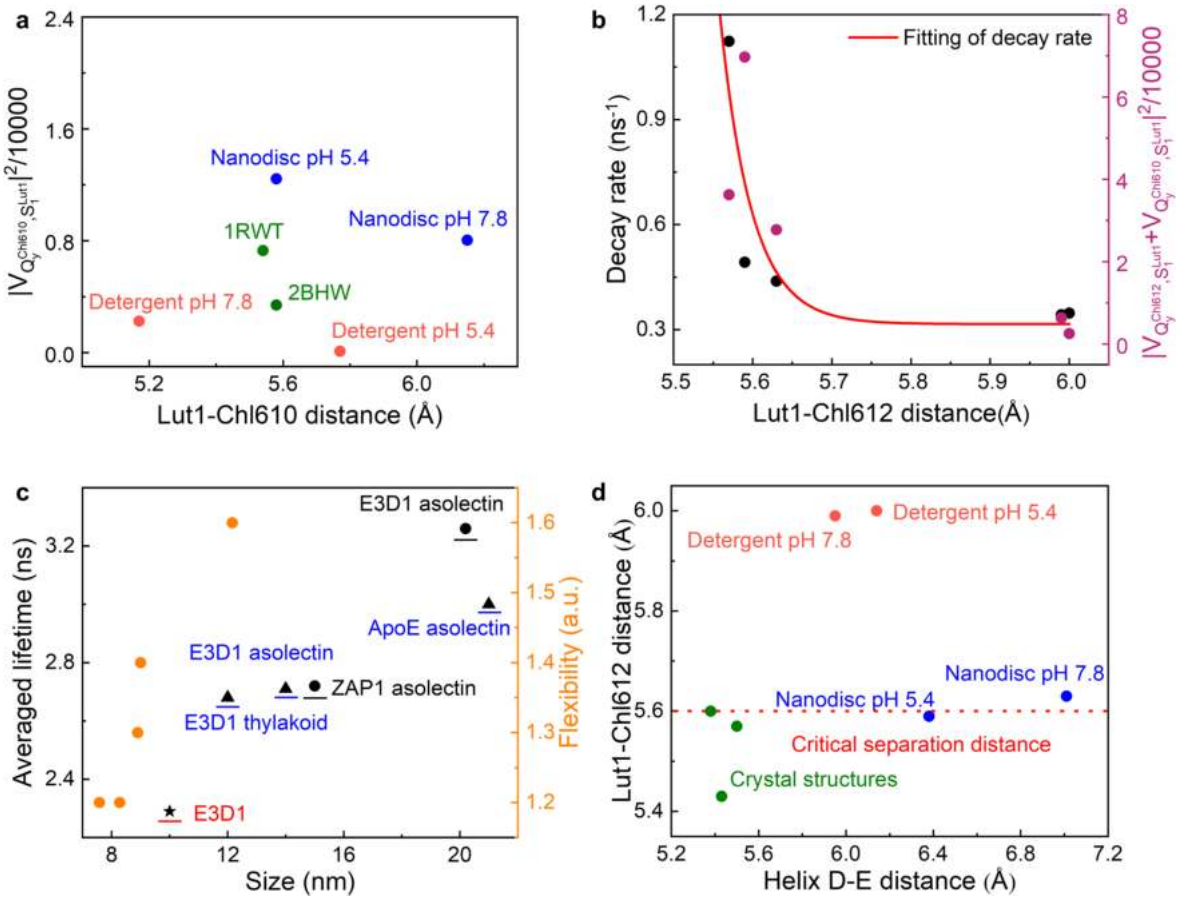

Extended Data Fig. 7 | Structural factors related to state transition at different conditions and their relationships. a, Plot of Lut1-Chl610 electronic coupling strength $|V_{Q_y^{Chl610},S_1^{Lut1}}|^2/10000$ against Lut1-Chl610 separation distance in different LHCII structures. **b**, Plots of the fluorescence decay rate (k = 1/fluorescence lifetime, black solid circles), the summed coupling strength $|V_{Q_y^{Chl612},S_1^{Lut1}} + V_{Q_y^{Chl610},S_1^{Lut1}}|^2/10000$ (purple solid circles) of Lut1–Chl612 and Lut1-Chl610 pairs against the Lut1-Chl612 separation distance (R), and the fitting equation is $k = 0.31 + 0.31e^{-25(R-5.6)}$. **c**, Plot of available fluorescence lifetime (black star represents the data from the current work, blue solid circles and triangles represent data from the literatures[38–40]) and flexibility (orange solid circles, data from the literature[44]) of LHCII in nanodisc against the corresponding nanodisc size. **d**, Plot of helix D-E distance against Lut1-Chl612 separation distance from different LHCII structures, red dotted line marks the critical separation distance of 5.6 Å, green solid circles represent the data from the crystal structures (PDB code: 1RWT, 2BHW).

https://doi.org/10.1038/s41477-023-01500-2

a

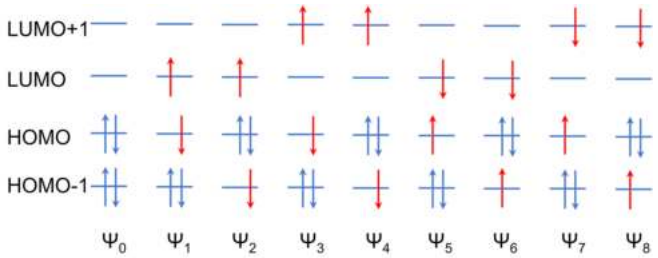

b

	MSDFT S_1(eV)	Ref.
Chlorophyll	1.72	1.75[70]
Lutein	2.02	1.91[71]

Extended Data Fig. 8 | Configurations and excitation energies for the first singlet excited states of the chlorophyll monomer and lutein monomer. **a**, Depiction of the minimal number of configurations necessary to model first singlet excited states of the chlorophyll monomer and lutein monomer. The ground-state configuration (Ψ_0) is shown along with eight spin-contaminated configurations (1–8). **b**, Excitation energies of chlorophyll and lutein and the reference values.

 https://doi.org/10.1038/s41477-023-01500-2

Extended Data Table 1 | Cryo-EM data collection, refinement and validation statistics of LHCII structures at different conditions

Conformations	Nanodisc pH 7.8	Nanodisc pH 5.4	Detergent pH 7.8	Detergent pH 5.4
Data collection and processing				
Magnification	22,500	22,500	22,500	22,500
Voltage (kV)	300	300	300	300
Electron exposure (e^{-} Å^{-2})	60	60	60	60
Defocus range (μm)	1.5-2.5	1.5-2.5	1.5-2.5	1.5-2.5
Pixel size (Å)	1.1	1.04	1.07	1.07
Symmetry imposed	C1	C1	C1	C1
Images (no.)	8,894	11,375	7,282	12,453
Initial particle images (no.)	5,123,887	6,256,638	3,583,010	5,436,117
Final particle images (no.)	817,473	860,690	653,924	648,142
Map resolution (Å)	2.64	2.63	2.59	2.68
FSC threshold	0.143	0.143	0.143	0.143
Refinement				
Model composition				
Initial model used (PDB code)	1RWT	1RWT	1RWT	1RWT
Model resolution (Å)	2.72	2.72	2.72	2.72
B factors (Å^2)				
Protein	24.12	23.71	26.50	24.06
Ligand	23.72	23.16	24.43	23.39
R.m.s. deviations				
Bond lengths(Å)	0.008	0.007	0.005	0.009
Bond angles (°)	1.564	1.645	1.280	1.682
Validation				
MolProbity score	1.74	1.98	1.79	1.91
Clashscore	11.96	13.71	11.05	12.63
Poor rotamers (%)	0.20	0.79	0.99	0.79
Ramachandran plot				
Favored	97.22	95.22	96.45	95.68
Allowed	2.78	4.78	3.55	4.32
Disallowed	0.00	0.00	0.00	0.00

https://doi.org/10.1038/s41477-023-01500-2

Extended Data Table 2 | Structural parameters for LHCII at different conditions. [&]: Protonated structures at pH 5.4. [*]: Data not available. [#]: Salt bridge separation distance, which are slightly affected by acidification. Data in bracket are the standard deviations of the average values

	Cryo-EM Structures				Crystal Structures		
Structures	LHCII nanodisc pH=7.8	LHCII nanodisc pH=5.4[&]	LHCII in detergent pH=7.8	LHCII in detergent pH=5.4[&]	1RWT	2BHW	Cucumber
Lifetime (ns)	2.28	2.03	2.92	2.88	0.89	/ [*]	/ [*]
State	Partially Quenched	Partially Quenched	Un-quenched	Un-quenched	Quenched	Quenched	Quenched
Lut1-Chl612 electronic coupling (cm^{-1})	76.9	152.6	32.3	40.8	105	217.6	/ [*]
Lut1-Chl610 electronic coupling (cm^{-1})	89.7	111.5	47.4	9.7	85.4	58.33	/ [*]
Salt bridge[#] R70-E180 (Å)	2.67 (0.33)	2.72 (0.14)	3.61 (0.26)	3.1 (0.24)	2.97 (0.07)	3.21 (0.05)	2.93 (0.08)
Salt bridge[#] E65-R180 (Å)	2.84 (0.46)	2.88 (0.29)	3.56 (0.30)	2.64 (0.23)	2.84 (0.12)	2.79 (0.03)	2.88 (0.10)
Lut1-Chl612 distance (Å)	5.63 (0.12)	5.59 (0.28)	5.99 (0.03)	6.00 (0.7)	5.54 (0.06)	5.43 (0.04)	5.60 (0.04)
Lut1-Chl610 distance (Å)	6.15 (0.14)	5.58 (0.27)	5.17 (0.05)	5.77 (0.14)	5.54 (0.05)	5.58 (0.01)	5.50 (0.05)
Helix D-E distance (Å)	7.01 (0.08)	6.38 (0.17)	5.95 (0.03)	6.14 (0.21)	5.5 (0.06)	5.42 (0.06)	5.38 (0.09)
Helix A-B crossing angle (deg)	121.9 (1.2)	117.9 (1.3)	119.3 (0.6)	116.6 (1.6)	117.4 (0.2)	116.4 (0.1)	117.3 (0.2)
Lut1-Lut2 crossing angle (deg)	80 (1.1)	76.7 (1.2)	82 (0.7)	75.1 (2.1)	73.4 (0.3)	74.6 (0.1)	73.2 (1.1)

nature portfolio

Corresponding author(s): Yuxiang Weng, Wei Ding, Jiali Gao

Last updated by author(s): Jul 24, 2023

Reporting Summary

Nature Portfolio wishes to improve the reproducibility of the work that we publish. This form provides structure for consistency and transparency in reporting. For further information on Nature Portfolio policies, see our Editorial Policies and the Editorial Policy Checklist.

Statistics

For all statistical analyses, confirm that the following items are present in the figure legend, table legend, main text, or Methods section.

n/a	Confirmed	
☐	☒	The exact sample size (*n*) for each experimental group/condition, given as a discrete number and unit of measurement
☐	☒	A statement on whether measurements were taken from distinct samples or whether the same sample was measured repeatedly
☒	☐	The statistical test(s) used AND whether they are one- or two-sided *Only common tests should be described solely by name; describe more complex techniques in the Methods section.*
☒	☐	A description of all covariates tested
☒	☐	A description of any assumptions or corrections, such as tests of normality and adjustment for multiple comparisons
☐	☒	A full description of the statistical parameters including central tendency (e.g. means) or other basic estimates (e.g. regression coefficient) AND variation (e.g. standard deviation) or associated estimates of uncertainty (e.g. confidence intervals)
☒	☐	For null hypothesis testing, the test statistic (e.g. *F*, *t*, *r*) with confidence intervals, effect sizes, degrees of freedom and *P* value noted *Give P values as exact values whenever suitable.*
☒	☐	For Bayesian analysis, information on the choice of priors and Markov chain Monte Carlo settings
☒	☐	For hierarchical and complex designs, identification of the appropriate level for tests and full reporting of outcomes
☒	☐	Estimates of effect sizes (e.g. Cohen's *d*, Pearson's *r*), indicating how they were calculated

Our web collection on statistics for biologists contains articles on many of the points above.

Software and code

Policy information about availability of computer code

Data collection	The cryo-EM data were collected using the EPU/SerialEM 4.0.19 automated data collection software package. The FTIR spectra were taken with vertex 70V (Bruker Optics, DE). The steady and transient fluorescence spectroscopy were taken with F-7000 spectrometer (Hitachi, JP) and streak camera. Absorption spectra were obtained using NanoDrop 2000c (Thermo Scientific).
Data analysis	cryoSPARC 4.0.0, PHENIX 1.20.1, Coot 0.9.4.1, Chimera 1.15 and PyMOL 2.4.0 were used to analyse cryo-EM data in this study, other spectra analysis was done using Origin 2019. The electronic coupling was determined by Qbics: a computational biology and chemistry software developed in the author's (JG) laboratory, and it can be accessed from https://qbics.info.

For manuscripts utilizing custom algorithms or software that are central to the research but not yet described in published literature, software must be made available to editors and reviewers. We strongly encourage code deposition in a community repository (e.g. GitHub). See the Nature Portfolio guidelines for submitting code & software for further information.

Data

Policy information about availability of data

All manuscripts must include a data availability statement. This statement should provide the following information, where applicable:

- Accession codes, unique identifiers, or web links for publicly available datasets
- A description of any restrictions on data availability
- For clinical datasets or third party data, please ensure that the statement adheres to our policy

The structures and cryo-EM maps have been submitted to PDB&EMDB and will be released upon publication. The respective PDB and EMDB codes are listed below:
Unprotonated structure of LHCII in detergent solution at pH 7.8: 8IWX, EMD-35782
Protonated structure of LHCII in detergent solution at pH 5.4: 8IWY, EMD-35783
Unprotonated structure of LHCII in detergent solution at pH 5.4: 8IWZ, EMD-35784
Unprotonated structure of LHCII in nanodisc at pH 7.8: 8IX0: EMD-35785
Protonated structure of LHCII in nanodisc at pH 5.4: 8IX1, EMD-35786
Unprotonated structure of LHCII in nanodisc at pH 5.4: 8IX2, EMD-35787

Human research participants

Policy information about studies involving human research participants and Sex and Gender in Research.

Reporting on sex and gender	n/a
Population characteristics	n/a
Recruitment	n/a
Ethics oversight	n/a

Note that full information on the approval of the study protocol must also be provided in the manuscript.

Field-specific reporting

Please select the one below that is the best fit for your research. If you are not sure, read the appropriate sections before making your selection.

☒ Life sciences ☐ Behavioural & social sciences ☐ Ecological, evolutionary & environmental sciences

For a reference copy of the document with all sections, see nature.com/documents/nr-reporting-summary-flat.pdf

Life sciences study design

All studies must disclose on these points even when the disclosure is negative.

Sample size	Statistical methods were not used to predetermine the sample size.
Data exclusions	The initial cryo-EM images are checked manually to exclude those with low contrast, thick ice or severe ice contaminations, which is a standard procedure for cryo-EM data processing. No spectral data have been excluded.
Replication	All spectral experiments were conducted three times for average.
Randomization	Randomization is not relevant to our study.
Blinding	Blinding is not relevant to our study because we tried to solve the structure of the specific protein.

Reporting for specific materials, systems and methods

We require information from authors about some types of materials, experimental systems and methods used in many studies. Here, indicate whether each material, system or method listed is relevant to your study. If you are not sure if a list item applies to your research, read the appropriate section before selecting a response.

Materials & experimental systems

n/a	Involved in the study
☒	☐ Antibodies
☒	☐ Eukaryotic cell lines
☒	☐ Palaeontology and archaeology
☒	☐ Animals and other organisms
☒	☐ Clinical data
☒	☐ Dual use research of concern

Methods

n/a	Involved in the study
☒	☐ ChIP-seq
☒	☐ Flow cytometry
☒	☐ MRI-based neuroimaging